Title
Ferroelastic Hysteresis in Thin Films of Methylammonium Lead Iodide

Permalink
https://escholarship.org/uc/item/02q89630

Journal
Chemistry of Materials, 33(1)

ISSN
0897-4756 1520-5002

Authors
Kennard, Rhys M
Dahlman, Clayton J
DeCrescent, Ryan A
et al.

Publication Date
2020-12-30

DOI
10.1021/acs.chemmater.0c03776

Peer reviewed

Ferroelastic Hysteresis in Thin Films of Methylammonium Lead Iodide

Rhys M. Kennard, [†] *Clayton J. Dahlman,* [†] *Ryan A. DeCrescent,* [‡] *Jon A. Schuller,* [‖] *Kunal Mukherjee,* [†] *Ram Seshadri,* [†+] *Michael L. Chabinyc* [†]*

† Materials Department, University of California, Santa Barbara, CA 93106, United States

‡ Department of Physics, University of California, Santa Barbara, CA 93106, United States

‖ Department of Electrical and Computer Engineering, University of California, Santa Barbara, CA 93106, United States

+Department of Chemistry and Biochemistry, University of California, Santa Barbara, CA 93106, United States

*Corresponding Author: mchabinyc@engineering.ucsb.edu

ABSTRACT

Mechanical strain can modify the structural and electronic properties of methylammonium lead iodide $MAPbI_3$. The consequences of ferroelastic hysteresis, which involves the retention of structural memory upon cycles of deformation, are reported for polycrystalline thin films of $MAPbI_3$. Repeatedly bent films were examined using Grazing Incidence Wide-Angle X-ray Scattering (GIWAXS) to quantitatively characterize the strains and proportions of twin domains. Approximate locations for the coercive stress and saturation on the ferroelastic stress-strain curve are identified, and changes to the stress-strain curve with cyclic strain are characterized. Notably, an external stress source, such as thermal stress from the substrate or a roll-to-roll printing setup, must apply at least |50| MPa to modify the proportions of different twins. The presence of specific twin domains is found to correlate to previously-reported strain and defect heterogeneity in $MAPbI_3$ films. Domains from differently-strained twin sets interact with each other. Long-term stability testing reveals that domain walls are highly immobile over extended periods. Nucleation of new domain walls occurs for specific mechanical strains and correlates closely with degradation. These results help to explain the behavior of ion migration, degradation rate, and photoluminescence in thin films under compressive and tensile strain.

INTRODUCTION

Hybrid halide perovskites of type $APbX_3$ have emerged as materials for solar cells and are attractive for a variety of other thin film electronic devices.[1–6] The highest power conversion efficiencies in solar cells have been achieved using compositional derivatives of tetragonal methylammonium lead iodide ($MAPbI_3$), by alloying MA^+ with Cs^+ and/or FA^+, or by alloying I^- with Br^-, to form $(Cs,FA,MA)Pb(Br,I)_3$.[1] Alloying of halides and introduction of large cations further provides a facile way to tune the band gap, making halide perovskites attractive for light emitting diodes or lasing applications.[3,5–10] A key advantage of halide perovskites over conventional semiconductors is the ease with which perovskites can coated via roll-to-roll processing to form electronic devices.[11] A thorough understanding of the structural consequences of repeated bending - i.e. repeated strain application - on perovskites is therefore crucial. To date, strain in $MAPbI_3$ films has been shown to affect defect concentration[12] and related properties such as degradation rate,[13,14] the activation energy of ion migration[13] and the photoluminescence lifetime.[15]

Tetragonal $MAPbI_3$ is ferroelastic, which complicates how it responds to mechanical strain. Ferroelasticity involves the spontaneous formation of sub-grain domains of differing orientation, the relative proportion of which can be changed by applying stress.[16–19] This phenomenon is common in a variety of materials, such as zirconia [20] or oxide and fluoride perovskites,[21,22] and has been increasingly investigated in halide perovskites.[23–32] At elevated temperatures many $APbX_3$ materials have higher symmetry, but as the material cools the R_4^+ phonon mode condenses, inducing permanent out-of-phase tilting of the BX_6 octahedra and a spontaneous strain in the material.[33–37] The strain magnitude is lowered by transition to a lower symmetry phase, which in $MAPbI_3$ is the cubic P*m*-3*m* to tetragonal I4/*mcm* transition.[16,17,37–42] Mechanical constraints such as surrounding grains encourage twin domain formation, thus ensuring that the original macroscopic dimensions are maintained. Such domains have previously been observed in $MAPbI_3$.[24,25,29–31] Compositional derivatives of $MAPbI_3$ that are thought to be cubic on the bulk scale (e.g. $(Cs,FA,MA)Pb(Br,I)_3$) also exhibit twinning on the nanoscale.[23] Although processing conditions may affect the types of domains formed, twinning is inherent to tetragonal $MAPbI_3$ and is therefore observed in films of this material. [30]

Applying stress to a ferroelastic induces ferroelastic hysteresis, which involves semi-reversibly changing the relative proportion of different domains ("domain switching") by inducing movement of the walls separating them.[18] Recent work shows that that the walls between twin domains in $MAPbI_3$ slow carrier diffusion in single crystals without any external strain applied.[43] Despite the increased attention paid to ferroelasticity in hybrid perovskites,[23,27,28,43–49] much still remains unknown. For example, in other materials, domain walls nucleate point defects and facilitate diffusion of ionic species.[50–53] Understanding how twin walls move and are created and annihilated is therefore crucial to the successful development of flexible $MAPbI_3$-based devices.

Here, we analyze the ferroelastic hysteresis loop of $MAPbI_3$ and its impact on the stability of polycrystalline films. Strain heterogeneity in previous reports that was linked to increased defect content was here found to originate from specific twin domains. Cyclic strain tests of films revealed the approximate stresses at which ferroelastic hysteresis initiated (coercive stress) and saturated, as well as the ways in which the stress-strain curve changed. The coercive stress revealed the thermal stress needed to change domain population, which was estimated for different substrates. Changes to domain sizes and proportions revealed changes to the number of domain walls and were correlated closely with enhanced degradation. This behavior was related to particular strain cycles, and can help explain differences in ion migration, degradation and photoluminescence lifetime behavior observed in literature.

RESULTS AND DISCUSSION

Identifying Sets of Twin Domains using GIWAXS.

We cast $MAPbI_3$ on polyimide (Kapton) and characterized the resulting films using Grazing Incidence Wide Angle X-ray Scattering (GIWAXS) (**Figure 1a**). PEDOT:PSS was cast to planarize the Kapton surface, and was selected because it is a widely-used hole transport layer in perovskite photovoltaic devices.[54,55] $MAPbI_3$ was then spin-cast following previously-described procedures (see **Experimental Methods**),[7] with an antisolvent rinse and 100°C annealing steps.[1,56] Scanning Electron Microscopy (SEM) (**Figure S1**) revealed that the $MAPbI_3$ film exhibited 200 ± 100 nm grain size and ≈ 400 nm thickness. PMMA was then cast on top of the $MAPbI_3$ to prevent degradation, [57] as subsequent experiments were largely performed in air. No X-ray scattering features of PbI_2 were observed (expected peak at $q \approx 0.9$ Å^{-1}; **Figure 1c**). The ring-like shape taken by the features in the 2D pattern (**Figure 1c**) indicates a distribution of orientations of $MAPbI_3$ crystallites, consistent with prior electron back scatter detection (EBSD) work on polycrystalline films.[58] To better understand correlations between these differing orientations and ferroelastic domains, small areas of the 2D GIWAXS patterns were integrated to form 1D patterns along two select orientations, near-in-plane (nIP) and near-out-of-plane (nOP) (**Figure 1c**). Details related to the analysis of the GIWAXS patterns are given in the **Experimental Methods** and in **Figure S2**. The large incidence angle (2°) was chosen so that the X-Rays penetrated the entire $MAPbI_3$ depth (calculated penetration depth 1000 nm; [59,60] **Figure 1a**); and observation of substrate peaks (**Figure**

1c) confirmed that the entire depth was probed. Because the GIWAXS beam area was several mm^2, the results below are representative of the bulk of the $MAPbI_3$ film.

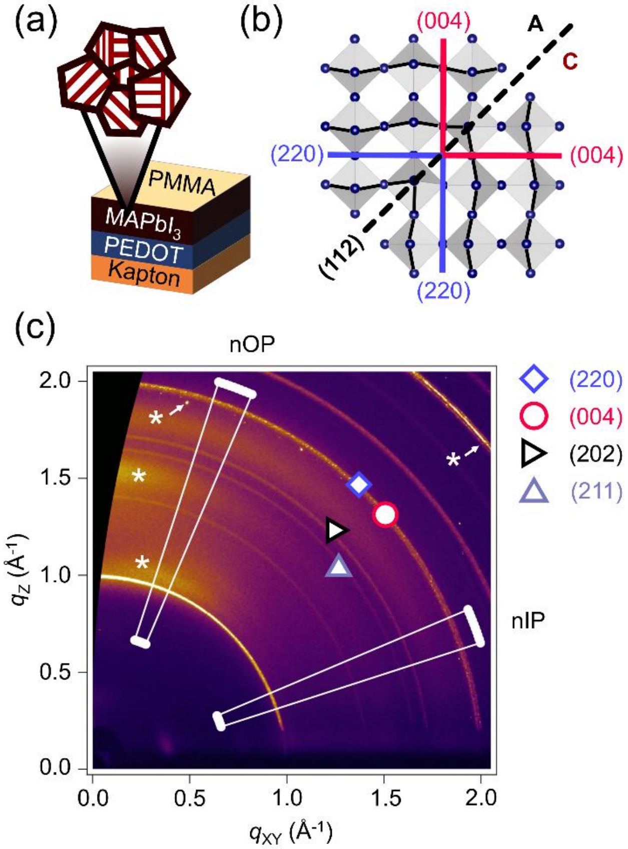

Figure 1. (a) Schematic of the samples as-prepared, with a Kapton substrate, a PEDOT: PSS planarization layer, $MAPbI_3$, and a PMMA encapsulation layer. GIWAXS X-Rays with incidence angle 2° penetrate roughly 1000 nm into the sample (throughout the whole $MAPbI_3$ film thickness), [59,60] over an area of several mm^2. (b) Twinning in $MAPbI_3$ grains, with crystallographic structure of two twin domains of $MAPbI_3$ following reference, [24] and with $MAPbI_3$ in the I4/*mcm* tetragonal phase.[24,37] The (220) and (004) planes are shown, as well as the (112) mirror plane (twin boundary/domain wall) separating the domains, and A and C twin types. (c) GIWAXS pattern of an as-cast $MAPbI_3$ film, showing the areas integrated for near-out-of-plane (nOP) analysis (18°-23°) and near-in-plane (nIP) analysis (67°-72°). The (220), (004), (202) and (211) rings are labelled. The asterisks correspond to substrate peaks (i.e. Kapton-PEDOT: PSS only; no $MAPbI_3$ or PMMA). Although appearing to overlap in this 2D pattern, the (220) and (004) peaks are distinguishable (see below).

The predominant twin domain structure and twin domain types observed by GIWAXS are shown in **Figure 1** and in **Figure 2**. At room temperature, $MAPbI_3$ is in the tetragonal I4/mcm phase,[37–42] with several ferroelastic domains cohabitating in the same grain (**Figure 1a-b**).[24,25,30] Previous Transmission Electron Microscopy (TEM) work [24] revealed that the (112) plane acts as a boundary between different domains (also called domain wall), and is also a mirror plane to these domains. Because we primarily saw ferroic *a* and *c* domain types (see below - **Figure 2**, **3**, **6**, **7**), we named the domains observed A and C. [61,62] To distinguish A vs. C, we used the scattering intensities and positions in reciprocal space of the (220) and (004) planes. The (220) nOP peak and associated (004) nIP peak revealed Domain A, while the (220) nIP peak and associated (004) nOP peak revealed Domain C (**Figure 1b**, **Figures 2-3**). However, the (220) and (004) planes have similar *d*-spacings in the 2D patterns (**Figure 1c**). For this reason, we additionally examined the evolution of the intensity of the (211) peak with respect to the (202) peak (see discussion of **Figure S3**). Importantly, the analysis of the intensities of the (220) vs. (004) peaks also allowed us to extract the relative fraction of Domains A vs. C in the film, and how this proportion changed after bending.

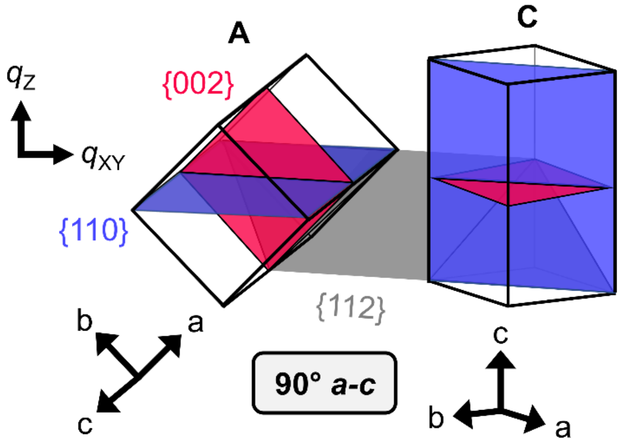

Figure 2. Summary schematic showing A and C domains, with preferential 90° *a*-*c* arrangement. [61,62]

Films that had not experienced mechanical deformation exhibited both A and C domain types (**Figure 3**). **Figure 3a** shows nOP and nIP patterns of an as-cast sample. The main nOP peak (near 3.14 Å) was assigned to a (220) plane, which is consistent with a higher intensity of the (211) peak appearing nOP (**Figure 3b**, see discussion of **Figure S3**). This preference for the nOP orientation of the (220) plane is consistent with what is typically observed for $MAPbI_3$ films. [31] In the nIP pattern, the peak near 3.16 Å was considerably more intense than in the nOP direction, and the (211) peak was much weaker, indicating less scattering from the (220) peak in the nIP direction. We therefore assigned the nIP peak near 3.16 Å to be the (004) plane that corresponds to crystallites with (220) planes oriented nOP. Based on these two assignments, there is a considerable population of A-type domains in the film. Thus, the typically-observed strong presence of (220) in films [31] corresponds to Domain A.

Since $MAPbI_3$ is a ferroelastic, twin domains exhibit the same crystal structure, but in different orientations. Therefore, the strains of (220) planes in different twinned domains should be equal. The nIP peak near 3.14 Å was thus assigned to (220) and the nOP peak near 3.16 Å was thus likely (004). These two peak assignments reveal Domain C. The two populations identified here, Domains A and C, are consistent with the well-established 90° *a*-*c* configuration, hence our nomenclature for the domains (**Figure 2**).[61,62] Further analysis of the domains required correcting the intensities for structure factor (see **Supporting Information**). We note that there were two other weaker peaks in this region, one near 3.12 Å and the other near 3.18 Å, with the latter being stronger in the nIP direction. The peak at 3.12 Å in particular appeared much more strongly after bending (**Figure 7a**). We thus appear to have two sets of twin domains: Twin Set 1 (TS1), that is dominant, with domains A:1 and C:1, and a smaller population of Twin Set 2 (TS2).

Correlating Strain Heterogeneity with Ferroelastic Domains.

We analyzed the strain of all peaks, allowing the assignment of peaks to TS2 (**Figure 3a, 3d**). The structure of I4/*mcm* $MAPbI_3$ in single-crystal form has been extensively studied, with broad agreement regarding lattice parameters at various temperatures. [37–42] Here, we selected the unstrained *d*-spacings at 300°K from a neutron-diffraction study of $MAPbI_3$ single crystals, chosen due to the precision of the method. [37] Strain was calculated based on shift from these unstrained *d*-spacings. To ensure consistency, we took patterns of four film samples and calculated average *d*-spacings and *d*-spacing uncertainties. For TS1, the (220) peak (near 3.14 Å), hereafter called “(220):1”, exhibited weak tensile strain ($+ 0.08 \pm 0.03$ %). The (004) peak in TS1 (near 3.16 Å, “(004):1”) exhibited compressive strain ($- 0.37 \pm 0.09$ %). It is expected that the (220) and (004) planes of domains A and C for TS1 exhibit the same strain, as these domains should only differ in their orientation. For TS2, based on the improbability of having domains with strains $\geq$ 1.5 %, we assigned the peak near 3.12 Å to the (220) plane and the peak near 3.18 Å to the (004) plane. Thus, for TS2, we have compressive strain ($- 0.39 \pm 0.13$ %) for (220):2, and large tensile strain ($+ 0.8 \pm 0.4$ %) for (004):2. The relative intensities of (220):2 and (004):2 roughly follow those of (220):1 and (004):1, likely indicating A and C domain types for TS2 as well, called A:2 and C:2. The strains from the (220) peaks for both twin sets are approximately a third of the magnitudes of the strains of the (004) peaks, and opposite in sign, matching what is expected from Poisson’s ratio of 0.33.[63] Thus, the strains identified are consistent with the film having two twin sets, each containing *a* and *c* type twin domains.

Importantly, we establish a correlation between the heterogeneity of strain in the films and the ferroelastic domains (**Figure 3d**). Sub-grain changes to strain and orientation were previously observed, but were not correlated with ferroelastic domains.[58] The *d*-spacings of the (220) peak were shown to vary by ≈ − 0.2 % within films, with the more compressed regions having higher defect densities.[12] Here, we show that variations in *d*-spacing in films correlate with different ferroelastic domains. Specifically, large compressive (220) strains originate from a different twin set. The large strains and small population of TS2 throughout the entire film thickness (**Figure 1a**) suggest that TS2 originates from unfavorable growth conditions such as rapid solvent removal, spatial constrains imposed by grain boundaries, and other factors. Because TS2 exhibits larger strains than TS1, it is more likely to appear in areas in which local strain is greater, such as near grain boundaries or at the substrate interface (**Figure 3d** and **7**). The films are dense with few pinholes (**Figure 1a**) and it is possible that TS2 may help offset strain gradients within the film.

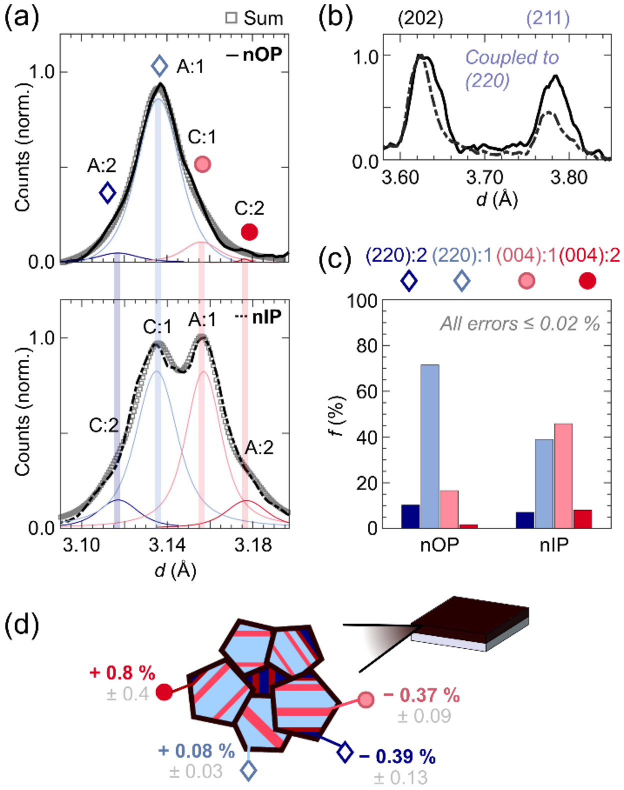

Figure 3. (a) GIWAXS near-out-of-plane (nOP) and near-in-plane (nIP) patterns of an as-cast $MAPbI_3$ film, with assignments to various (220) or (004) and twin domain type labelled. nOP and nIP patterns are normalized to highlight the relative contributions of different (220) and (004). Each fit is shown individually, as is the sum of the fit peaks. (b) (202)-(211) region of the nOP and nIP patterns (see **Figure S3**), normalized with respect to the (202) for (211) intensity comparison. (c) Fraction *f* of the film exhibiting the different (220) and (004) orientations nOP and nIP for the patterns in (a). Average fractions for 4 samples are shown in **Figure S4**. (d) Summary schematic of the sub-grain twinning microstructure identified here, with two possibilities for Twin Set 2 location (separate small grains and boundaries of grains that are predominantly Twin Set 1). Strains associated with the (220) and (004) peaks are listed (calculated from peak shifts from the single crystal structure at 300°K [37]) and were calculated from the average and standard deviation for 4 samples.

Determining Volume Fractions of Ferroelastic Domains.

Next, we calculated the relative fraction *f* of each domain in the film (see **Supporting Information**). The fractions for the patterns shown in **Figure 3a** are shown in **Figure 3c**, and the averaged fractions for four samples are shown in **Figure S4**. We distinguish two fractions *f*, obtained respectively from the nOP and nIP patterns. The distinction is necessary, as nOP scattering detects most planes parallel to the substrate; however, nIP scattering can miss a significant number of planes perpendicular to the substrate (**Figure S5**), in crystallites that otherwise have nOP planes visible. Thus, we extract volume fraction from the nOP patterns, and use the nIP patterns to qualitatively confirm our interpretations. The large incidence angle (2°) means the entire film thickness is considered (**Figure 1**).

From the nOP pattern (**Figure 3a**), ≈ 70 % of the film exhibits (220):1, with ≈ 20 % of the film exhibiting (004):1 and another ≈ 10 % exhibiting some combination of (220):2 and (004):2, with a greater amount of (220):2 (**Figure 3c**). This confirms the predominance of A-type domains. The results in **Figure 3** were also reproduced for 3 subsequent films, with between 80-100% of fractions *f* from the nOP patterns belonging to TS1, and the remaining 0-20 % being TS2 (**Figure S4**). Analysis of nIP patterns revealed ≈ 45 % and ≈ 40 % for the (004):1 and (220):1 respectively, in agreement with both 80-100 % of the film being TS1, and with there being some invisible peaks nIP (**Figure S5**). Some of the lack of agreement between nOP and nIP fractions could also originate from the grains being rotated in-plane with respect to each other. Another possibility is that we have some 90° *a-a* twinning, involving two A-type domains, where the domain wall belongs to the {112} family. This 90° *a-a* configuration is the structural equivalent of the 90° *a-c* configuration (**Figure 2**), but with a different orientation.[62] Prior work reported 90° *a-a* configuration for films cast directly on TEM grids,[24] rather than the predominant 90° *a-c* configuration observed here under different growth conditions. To circumvent questions of nIP plane invisibility vs. in-plane grain rotation vs. of 90° *a-c* / 90° *a-a* twinning type, we restrict quantitative analysis of fractions to the nOP patterns. Overall, the films are 80-100% TS1 and 0-20 % TS2, with a preference for 90° *a-c* twinning type (**Figure 2**, **3d**).

Residual Stress in $MAPbI_3$ *Films on Flexible Substrates.*

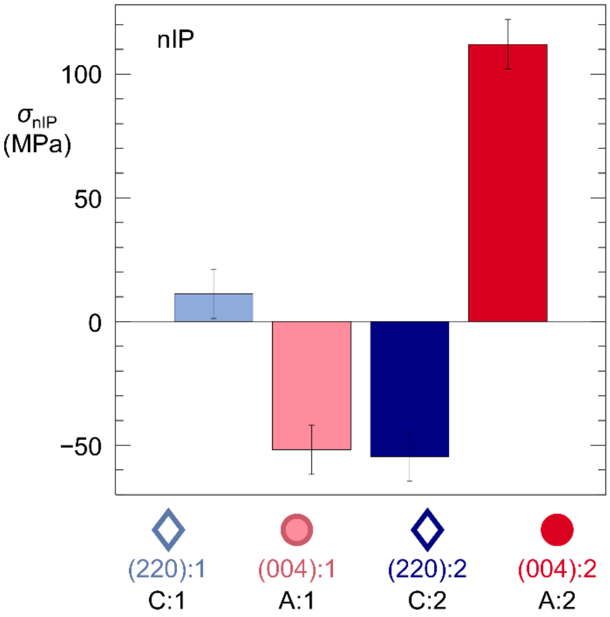

Figure 4. Conversion of the strains of (220):1, (004):1, (220):2 and (004):2 to stresses, with the corresponding nIP twin domains labelled. All error bars refer to the standard deviation from 4 samples.

Because the impacts of thermal stress from the substrate have garnered much interest, [13,14,64] we also quantified the nIP stresses of the four domains (**Figure 4**). We multiplied the strains identified for (220):1, (004):1, (220):2 and (004):2 (C:1, A:1, C:2 and A:2, nIP) by the Young's modulus for $MAPbI_3$ (14 GPa, chosen to be mid-range among reported values) and plotted these stresses in **Figure 4**. [63,65–67] Because the modulus is nearly directionally isotropic, [67] we multiplied the strains by the same modulus for (220) and (004) values to get the nIP stresses. These stresses were 11, − 52, − 55 and 112 (± 10) MPa for (220):1, (004):1, (220):2 and (004):2 respectively. As discussed above (**Figure 1a**), these are representative of the entire film depth. In prior work, switching from a silicon substrate with low thermal expansion coefficient or T.E.C. (0.26×10^{-5}/K) to a polycarbonate substrate with similar T.E.C. (6.5×10^{-5}/K) to those reported for $MAPbI_3$ ($4\text{-}16 \times 10^{-5}$/K) [68,69] was reported to greatly reduce the average residual in-plane stress, as measured via wafer curvature. [14] However, the contributions of individual twin domains to this stress were not elucidated. Here, we have a Kapton substrate (T.E.C. $3\text{-}11 \times 10^{-5}$/K) [70,71] and PEDOT: PSS planarization layer (T.E.C. 5×10^{-5}/K), [72] with similar T.E.C. to $MAPbI_3$ ($4\text{-}16 \times 10^{-5}$/K), [68,69] and a PMMA capping layer that also has similar T.E.C. ($5\text{-}10 \times 10^{-5}$/K). [73] Because $\text{T.E.C.}_{\text{Kapton/PEDOT: PSS}} \approx \text{T.E.C.}_{\text{Polycarbonate}}$ and because the films in prior work [14] were also processed at 100°C, we compared the individual domain stresses to the reported average stress of $MAPbI_3$ on polycarbonate (12 ± 2 MPa). With the exception of the (220):1, all of the individual domain stresses exhibited much larger magnitude than the average stress of $MAPbI_3$ on polycarbonate, with some exhibiting opposite sign. Notably, most individual domain stress magnitudes were of equal or larger magnitude to the average stress reported for $MAPbI_3$ on Si (54 ± 8 MPa). These results demonstrate that the residual stresses of individual twin domains in $MAPbI_3$ can be quite large even when using a substrate of similar T.E.C..

Expected Ferroelastic Behavior upon Bending and Experimental Design.

The ferroelastic hysteresis loop for $MAPbI_3$ has not yet been characterized in detail. Therefore, we analyzed structural changes caused by repeated bending, which is of interest for the behavior flexible devices. We will first describe expected ferroelastic behavior (**Figure 5**), then discuss the effects of repeated bending on film structure (**Figures 6**,**7**,**8**) and stability (**Figure 9**). We then relate our findings to existing literature on defect behavior in $MAPbI_3$, as domain walls have been found to nucleate vacancies and facilitate ion diffusion in other materials.[50–53]

Ferroelastic hysteresis involves non-linear, but to limited extent, reversible switching from one domain type to another; in our case, from domain A to domain C (**Figure 5a**). [18,74] This is accomplished by applying tensile strain (or stress) in q_X, which causes the domain wall to move, provided that the applied stress has some minimum magnitude corresponding to the coercive stress σ_C. Thus, the bond distances between the Pb^{2+} ions and the I^- ions change *at the domain wall, on the side of domain A*, such that eventually the octahedral tilting of domain C *at the domain wall* becomes more energetically favorable. [18] The domain wall thus advances through A and converts all the octahedral tilting to that of C. Correspondingly, the orientations of the (220) and (004) planes become that of C. If the material is under an opposite (compressive) stress in q_X, the octahedral tilting of A becomes again more favorable, so the domain wall moves back through C and A becomes bigger. Thus, while being somewhat reversible, the process is highly non-linear (**Figure 5b**), and the domain sizes after a full ferroelastic hysteresis loop may not be the same as they were initially. Saturation S (**Figure 4b**) is achieved when all possible switching to either A or C has occurred. Domain switching also imparts an inelastic strain ε_i on the material [20,21] that is retained after the applied strain is removed. This retention enabled us to indirectly analyze the ferroelastic hysteresis loop.

Ferroelastic hysteresis is one part of the stress-strain curve for ferroelastics. An idealized curve based on the literature for various oxide perovskites and zirconia is presented in **Figure 5c**. [20–22,75] Upon fabrication, a spontaneous strain ε_S exists in the material. At very low applied stresses (between point 1 and σ_C), there is an elastic-only regime, in which the domain walls do not move and bonds between atoms simply stretch or compress. At the coercive stress σ_C, ferroelastic hysteresis begins (**Figure 5b-5c**). In this regime, the types of strains acquired by the material are assigned differently from study to study; [20–22] but it is generally agreed that ferroelastic hysteresis imparts inelastic strains on the material, which for simplicity, we call the inelastic strain ε_i. The end of the ferroelastic hysteresis regime is marked by saturation *S*, at which point all possible domain switching has occurred. After this ferroelastic regime, a second mostly-elastic regime (until point 2) occurs, followed by the fully plastic regime (points 2-3) and fracture. For applied stresses below the fully plastic regime, the total strain in the material is $\varepsilon_{tot} = \varepsilon_{Elastic} + \varepsilon_i$; where $\varepsilon_{Elastic}$ is elastic strain and ε_i is the inelastic strain. Some ferroelastics exhibit large plastic regimes, [20] others less so, [21,22] indicated by two possible locations for fracture. Experiments on free-standing $MAPbI_3$ films identified only a single mostly-linear elastic regime before fracture. [76] This indicates 1) that that the fully plastic regime is likely quite small and 2) that the slopes both quasi-elastic regimes and the ferroelastic hysteresis regime are likely quite similar. In **Figure 5c**, we have drawn them to be very different for clarity. For any stress larger than σ_C, if the applied stress is removed ("Unloading" in **Figure 5c**), the material does not go back to its initial state, due to the inelastic strain ε_i. Subsequent re-loading occurs much more closely to the Unloading (dashed) line in **Figure 5c** than to the original curve. In the following experiments, we focus particularly on the unloading/re-loading behavior to indirectly study the hysteresis loop.

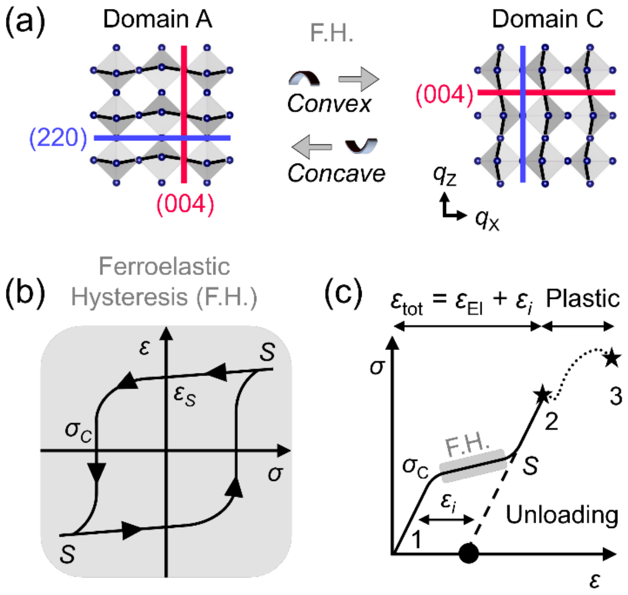

Figure 5. (a) Expected structural changes during ferroelastic hysteresis; tetragonal crystal structure from reference.[37] *Convex* bending applies tensile in-plane strain and *concave* bending applies compressive in-plane strain. (b) Ferroelastic hysteresis loop and (c) Idealized stress-strain curve for a ferroelastic based on prior work,[20–22] where ε_S, ε_i, ε_{tot}, $\varepsilon_{Elastic}$ are the spontaneous, inelastic, total and elastic strains respectively, *S* is the saturation point, and σ_C is the coercive stress. The stars indicate fracture point locations for different materials. GIWAXS patterns were collected after unloading the applied stress (black dot on the stress-strain curve).

The bending experiment is schematically shown in **Figure S7**, and referenced in **Figure 5a.** The $MAPbI_3$ stack was repeatedly bent around cylinders and then released, with two different bending configurations used. Following the naming convention used in prior works, [13–15] *convex* bending ("outward" bending) involves having the Kapton substrate touch the cylinder, with $MAPbI_3$/PMMA on the outside, and *concave* bending ("inward" bending) involves having $MAPbI_3$/PMMA touch the cylinder with Kapton on the outside (**Figure 5**, **S7**). Thus, strain ε_X is applied along q_X, and strains ε_Y and ε_Z are induced in q_Y and q_Z, following the coordinate system of **Figure S7**. Convex bending results in tensile ε_X (compressive ε_Y and ε_Z) and concave bending results in compressive ε_X (tensile ε_Y and ε_Z). Several bending diameters were selected and the applied strains $|\varepsilon_X|$ were calculated following the methodology outlined in the **Supporting Information**.[63,65–67,77–79] Using Poisson's ratio (0.33), [63] the induced strains $|\varepsilon_Z|$ in q_Z were then approximated (**Table 1**). We verified via SEM that applying these strains did not cause readily observable fracture of the films (**Figure S8**). Prior to bending, the film was isotropic in-plane, as the small thermal expansion mismatch between the polymer substrate (T.E.C. 3-11 × 10^{-5}/K, [70,71]) and $MAPbI_3$ (T.E.C. 4-16 × 10^{-5}/K, [68,69]) induced a mild biaxial in-plane strain. We collected GIWAXS patterns immediately after the applied strain was relieved, i.e. after "Unloading" (**Figure 5**), and we call these post-bending samples "unbent".

Diameter (mm)	$\mid \varepsilon_X \mid$ (%)	$\mid \varepsilon_Z \mid$ (%)
35	0.34	0.10
31	0.39	0.12
18	0.67	0.20
10	1.26	0.41
4.1	3.06	1.01

Table 1. List of diameters employed and the corresponding applied strains $|\varepsilon_X|$ and induced strains $|\varepsilon_Z|$ to the q_X and q_Z directions respectively.

Sweeping Through the Ferroelastic Hysteresis Loop by Bending.

Bending with a diameter of 10 mm (**Figure 6**) induced clear signatures of ferroelastic hysteresis. **Figure 6a** shows the evolution of the nOP patterns of a film after up to 12 *convex* bending cycles around a 10 mm diameter. Following this, the film was bent *concavely* up to 12 times. After *convex* bending, the initial (220):1 intensity decreased, in favor of the (004):1 intensity increasing. Subsequent *concave* bending restored the (220):1 intensity. These observations were backed by quantitative analysis of the fractions for all peaks (**Figure 6b**) and by the decrease (*convex* bending) then increase (*concave* bending) of the (211) intensity (**Figure S9**). Thus, A:1 domains were replaced by C:1 domains upon *convex* bending, and this process was generally reversed upon subsequent *concave* bending. However, the strong retention of (220):1 intensity (**Figure 6a-b**) suggests that the domain walls did not move very far. Some changes in (220) and (004) strains were observed after bending; however, the origins of these were not clear (see discussion of **Figure S12**).

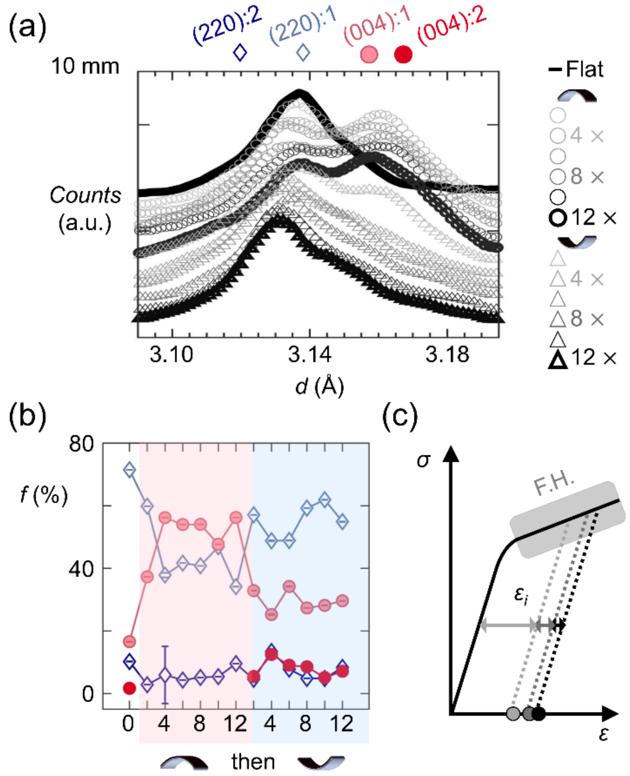

Figure 6. 10 mm bending experiment. (a) GIWAXS nOP patterns in the (004)-(220) region for the successive *convex* and *concave* bending around a 10 mm diameter. For the (220):1, (004):1, (220):2 and (004):2 peaks in these patterns, (b) corrected fractions *f* of the total scattered intensity in the peaks from (a). (c) Relationships between the observed domain switching and the stress-strain curve.

The changes observed can be correlated with the stress-strain curve, shown in **Figure 6c**. In cycles 4-12 for both *convex* and subsequent *concave* bending, the fractions plateaued at consistent values (**Figure 6b**), indicating that after cycle 4, the amount of A vs. C was stable. This suggests that during the first *convex* bending, $MAPbI_3$ followed the initial stress-strain curve, and the A:C domain ratio changed. When the applied stress was removed, the curve followed the unloading line (dashed). Subsequent re-loading and unloading occurred in a similar location to the first unloading line, leading to the plateau in the fraction of each domain. During subsequent *concave* bending, the domain walls moved closer to their original positions, and the unloading/reloading lines moved closer to the original curve.

We next applied larger strains to $MAPbI_3$ films. The bending experiment was repeated with a diameter of 4.1 mm ($|\varepsilon_X| = 3.06$ %; $|\varepsilon_Z| = 1.01$ %; **Figure 7**). Separately, we investigated the effects of *concave* bending only, without prior *convex* bending. The changes to the (220):1 and (004):1 peaks (**Figure 7a**) were more pronounced than for the 10 mm experiment, likely due to the larger applied strain (see also **Figure S10**). Interestingly, the (220):2 appeared much more distinctly after *convex* then subsequent *concave* bending, suggesting some interaction between TS1 and TS2 (see discussion below).

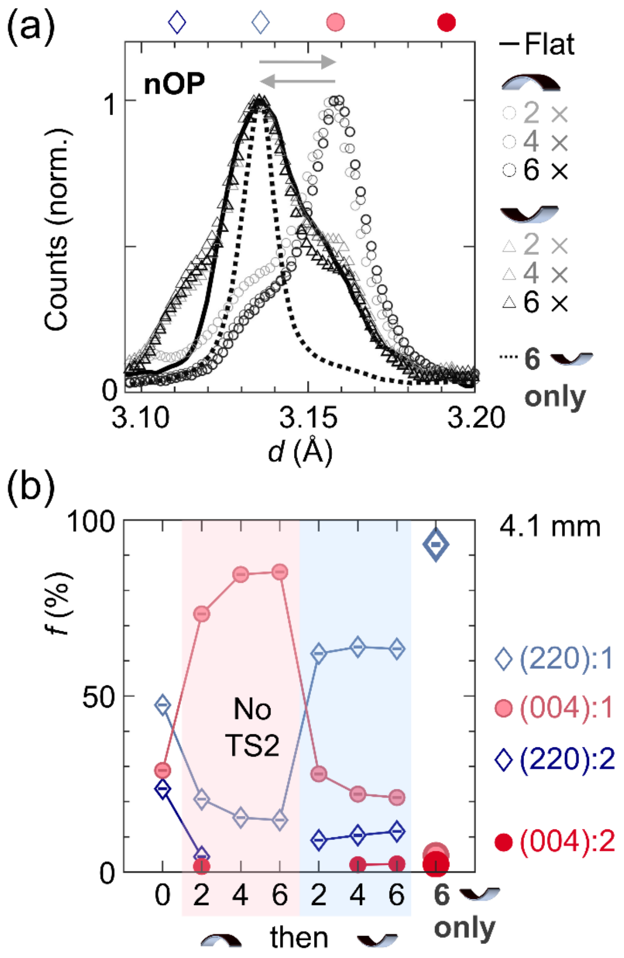

Figure 7. 4.1 mm bending experiment. (a) nOP patterns and (b) Corrected fractions of total scattered intensity *f* (uncertainties < 0.1 %) for nOP peaks in the (220)-(004) region, for 6 *convex* followed by 6 *concave* bending cycles, and 6 *concave* bending cycles only.

Saturation was nearly attained upon bending around a 4.1 mm diameter (**Figure 7a**). As-cast, the film exhibited the typical preference for A:1 ((220):1 nOP), with some C:1 ((004):1 nOP) and A:2 ((220):2 nOP). *Convex* bending increased the C:1 population to ≈ 85 % of the film, accompanied by a large decrease in the A:1 fraction and complete disappearance of A:2. No fracturing was observed **(Figure S8)**. This process was to some extent reversed with *concave* bending, with A:1 ((220):1) occupying ≈ 65 % of the total nOP population, which is still higher than the as-cast A:1 population (≈ 50 %). A:2 reappeared, much more distinctly, although at slightly lower fraction than for the as-cast sample. Strikingly, concave-only bending induced near-complete (95 %) A:1 population nOP, indicating near-complete saturation. These trends in the fractions suggest near-complete cycling through the hysteresis loop, and certainly to greater extents than for the 10 mm diameter.

Removing Large Compressive Strains.

The evolution in fractions f for TS2 suggested interaction between TS1 and TS2 (**Figure 7**), and therefore, physical contact between them. TS2 disappeared after 4 *convex* cycles and reappeared very distinctly after subsequent *concave* bending. Because the entire film depth was probed (**Figure 1**), this suggests either the presence of a mobile domain wall between TS1 and TS2, or that small grains of TS2 only can be converted to the more favorable TS1 using very large applied strains ($|\varepsilon_X| \approx 3.06$ % here). In support of these interpretations, the compressively-strained A:2 disappeared completely after 6 *concave* cycles only (induced tensile $|\varepsilon_Z|$), in favor of A:1, which has mild tensile strain. Thus, the ratio of TS1: TS2 can be controlled by applying large strains.

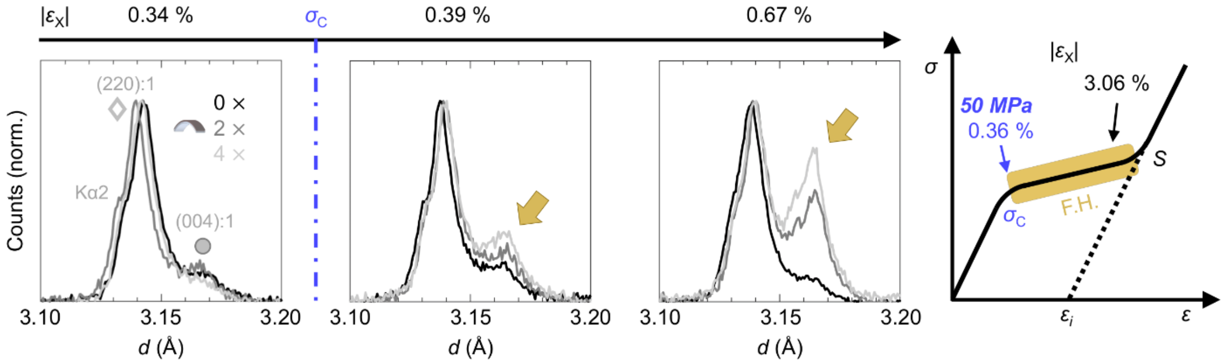

Figure 8. Determination of the coercive strain, from which the coercive stress σ_C was calculated. Powder XRD data for the 35 mm, 31 mm and 18 mm-diameter bending experiments, corresponding to applied $|\varepsilon_X|$ of ≈ 0.34 %, 0.39 % and 0.67 % respectively. The location of the coercive stress on the stress-strain curve is shown on the right. The yellow arrows show growth of the (004):1, indicative of ferroelastic hysteresis (F.H.).

Finally, we repeated the bending experiment with much larger diameters, to find the coercive stress (**Figure 8**). Because (004):1 grows into a peak that is very distinct from (220):1 **(Figure 6, 7)** we were able to use powder X-Ray diffraction (PXRD), rather than GIWAXS. Due impurities in the X-Ray wavelength (Cu-Kα2, tungsten and Cu-Kβ) resulting in extra peaks, and due to the low counts on the powder diffractometer, TS2 could not be resolved as easily; however, the onset of hysteresis was clearly identified using the TS1 peaks. The PXRD patterns of films bent convexly up to 4 × around diameters of 35 mm, 31 mm and 18 mm are shown in **Figure 8**, with applied strains $|\varepsilon_X|$ of ≈ 0.34 %, 0.39 % and 0.67 % respectively. The patterns shifted slightly and inconsistently in *d*-spacing after bending. This is likely caused by the lack of height alignment of the flexible films in PXRD, which is done in GIWAXS and necessary to obtain accurate *d*-spacings. Notably, the (004):1 did not grow when $|\varepsilon_X| \approx 0.34$ %, grew noticeably when $|\varepsilon_X| \approx 0.39$ %, and grew significantly when $|\varepsilon_X| \approx 0.67$ %. A control experiment was performed to confirm that these changes were not induced by the X-Ray beam (**Figure S11**). Thus, the coercive strain is $|\varepsilon_X|$ ≈ 0.36 % Because the actual applied strain is in q_X, we take $|\varepsilon_X|$ to calculate the coercive stress. Using a modulus of 14 GPa, [63,65–67] the coercive stress for $MAPbI_3$ is thus $\sigma_C \approx 50$ MPa.

Using Substrate Thermal Mismatch to Control the Population of Twins.

If an external stress source, such as thermal stress from the substrate or roll-to-roll printing setup, causes application of more than the coercive stress, |50| MPa in ε_X (**Figure 8**), it will modify the twin domain population. The stress σ_T imparted by thermal mismatch can be calculated using $\sigma_T = \frac{E_P}{1-\upsilon_P}(\alpha_S - \alpha_P)\Delta T$, [14] where E_P is the Young's modulus, υ_P is the Poisson's ratio, α_S and α_P are the T.E.C.s of the substrate and the perovskite and ΔT is the temperature gradient while cooling. Using the values discussed in the Residual Stress section, (E_P = 14 GPa, υ_P = 0.33, $\alpha_P \approx$ 5×10^{-5}/K and ΔT = 100°C − 20°C = − 80°C), a low T.E.C. substrate such as silicon (α_S = 0.26 $\times 10^{-5}$/K) will induce ≈ 50 MPa on $MAPbI_3$ for a low annealing temperature of 70°C. A glass substrate with mid-range T.E.C. (α_S = 1 × 10^{-5}/K) will induce the coercive stress upon cooling from 80°C and finally, a substrate with a higher T.E.C. such as Kapton (α_S = 3 × 10^{-5}/K, chosen among the lower reporter T.E.Cs for Kapton) [70,71] will induce the coercive stress upon cooling from 140°C. These numbers will vary based on the E_P and T.E.C. selected for the calculation; however, it is clear that ferroelastic behavior should be quite different with substrates of differing T.E.C. Thus, it does seem that thermal mismatch can be used to tailor the ferroelastic domain population. However, this does not exclude interface interactions or other solution-casting phenomena [80] which may also greatly direct twin population. Further work is needed to decouple these effects.

***Domain Walls and Long-Term Stability*.**

We also examined the long-term stability of films with no bending, and either 6 *convex* cycles only or 6 *concave* cycles only around the 4.1 mm diameter (**Figure 9**). We stored these films for 7 months in ambient and in the dark, and then examined powder XRD patterns. Specifically, we looked for the appearance of the degradation product PbI_2 at $d \approx 7$ Å (**Figure 9a**) and for major changes in the proportions of A:1 vs. C:1 (**Figure 9b**). Due to low signal on the powder diffractometer, TS2 was not easily resolvable. Prior *convex* bending only correlated with a large amount of PbI_2, while no bending and *concave* bending only showed no PbI_2 (**Figure 9a**). In addition, the patterns in the (220)/(004) region (**Figure 9b**) were quite similar to those 7 months prior (**Figure 7a**), suggesting that the proportions of A:1 vs. C:1 changed negligibly over 7 months (**Figure 9b**). Thus, without external stimulus, the domain walls appear to be fairly immobile.

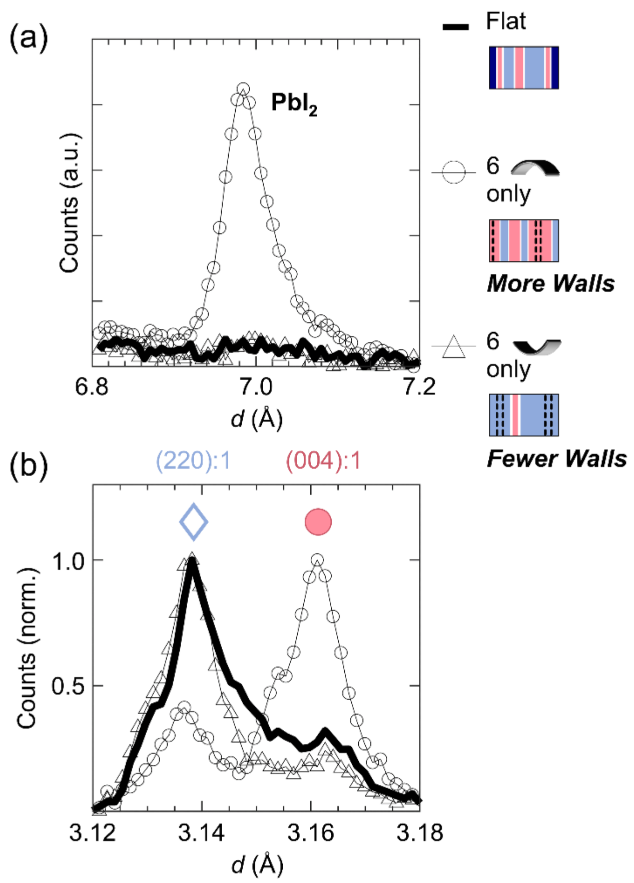

Figure 9. Powder XRD patterns of non-bent films (flat) and films previously bent *convexly* and *concavely* around a 4.1 mm diameter, after 7 months of storage in air, showing (a) the region in which the degradation product PbI_2 typically appears and (b) the (220)/(004) region. Schematics are shown of twin domain layout prior to storage (see **Figure S13**), with the dashed lines indicating ghost walls.

We noticed an interesting correlation between these differences in degradation, and creation vs. annihilation of domain walls. Analysis of peak widths after bending (4.1 mm experiment – **Figure S6** and **S13**) indicated wall creation during *convex* bending and annihilation during *concave* bending. This analysis (see discussion of **Figure S6** and **S13**) is consistent with observations in literature from polarized optical microscopy of $MAPbI_3$.[30] Indeed, the as-cast films contained few C domains, so nucleation of new C domains might be necessary to accommodate all the applied strain during *convex* bending. In contrast, because *concave* bending favors the presence of A domains and because the as-cast films contained mostly A domains, existing A domains grew and merged into a few large domains without the need of domain nucleation. Thus, walls seemed to be created during *convex* bending, with more degradation occurring after bending in this configuration (**Figure 9**). In contrast, films with no changes in number of walls or annihilation of walls were stable.

More walls likely correlates with more degradation because walls encourage point defect presence. In other systems, walls are known to harbor a higher concentration of vacancies and to facilitate diffusion of vacancies/ionic species.[50–53] Domain walls can also nucleate point defects,[81] so the walls nucleated during *convex* bending may have also nucleated more point defects. However, walls may also have moved during *convex* bending. When they move, domain walls can leave behind some of the vacancies they contain, creating a "ghost line" of vacancies in the old wall location, also sometimes called "ghost wall".[50] This can create a "memory" of the wall,[82,83] which has been observed several times in $MAPbI_3$.[24,29] This memory could mean that wall movement or annihilation does not fully remove the point defects residing in the previous location of the wall. Here, we found that the films with likely wall nucleation (*convex* bending) showed PbI_2 formation; while the films for with wall annihilation or movement only (*concave* bending) showed no PbI_2 formation. Additionally, films for which no wall movement was imposed, also showed no PbI_2 formation. This result implies that additional point defects, created during the wall nucleation in *convex* bending, are responsible for the enhanced degradation. In contrast, wall movement, lack thereof, or annihilation do not nucleate new defects, so films with *concave* or no bending showed no bulk degradation.

Impact for Behavior of Optoelectronics.

Wall creation during *convex* bending and wall annihilation during *concave* bending help explain prior defect-related results in $MAPbI_3$.[13–15] Prior studies found that films maintained under *convex* bending exhibited lower activation energy for vacancy-mediated ion migration[13] and more PbI_2 formation (i.e. degradation),[13,14] than flat films, suggesting higher defect content. Correspondingly, the photoluminescence lifetime of $MAPbI_3$ films decreased during *convex* bending in a different study,[15] suggesting more trap-mediated recombination. Our analyses (**Figures 7**, **9**, **S13**) indicate that these behaviors originate from domain wall nucleation during *convex* bending. The opposite trends regarding degradation, ion migration, and photoluminescence lifetime were observed for *in-situ concave* bending, suggesting fewer point defects/ domain walls (**Figures 7**, **9**, **S13**). Our results also indicate that repeated bending in one configuration (*convex* or *concave*) will likely not change the above-described behaviors much after the first few bending cycles (**Figure 6** and **Figure 7**). In addition, domain walls will not move without external stimulus (**Figure 9**). Subsequent bending in the opposite configuration (i.e. *concave* or *convex*) will change these defect behaviors to limited extents (**Figure 6** and **Figure 7**). To avoid such defect-related changes, the films should not be bent past the coercive stress (≈ 50 MPa, **Figure 8**), which is likely most relevant in the context of roll-to-roll processing $MAPbI_3$, or installing flexible modules. Thermal control over twin population may be employed using low-TEC substrates and mild temperatures (**Using Substrate Thermal Mismatch to Control the Population of Twins** section; **Figure 8**). A possible method for eliminating unfavorably-strained domains (compressive A:2 domains, **Figure 3**) and reducing the number of domain walls is to apply large out-of-plane tensile strain (**Figure 7**).

Changing the number of twin walls in films upon repeated bending may greatly impact carrier diffusion. Our findings reveal twin wall movement, and strongly suggest wall creation, annihilation, and the presence of “ghost walls” [24,29,50,82,83] in the sample after bending, which is a memory of the wall formed by the point defects the departed wall has left behind. Deep traps seem to nucleate along with twin walls *in films*, as evidenced by the decreased photoluminescence lifetime upon *convex* bending (i.e. enhanced trap-mediated recombination).[15] In apparent contrast, recent work on single crystals suggests that twin walls contain shallow traps that slow carrier diffusion, but do not induce trap-mediated recombination.[43–45] It is possible that single crystals contain fewer deep traps than films, and thus that twin walls impact carrier diffusion very differently in films vs. single crystals. It is also not clear to what extent twin walls carry their traps with them when they move or annihilate. “Ghost walls” may therefore greatly impact carrier transport in both films and single crystals. The impacts of repeated bending on shallow trapping and carrier diffusion requires further investigation, particularly in films.

We note that the detailed ferroelastic loop will also depend on factors such as the grain size. In oxide perovskites, grain size is known to affect domain/domain wall formation.[84] Here, we used films with grains of 200 ± 100 nm, but films used in devices can have grain sizes of up to several microns,[85] which may affect the types of twin domains formed and their strains. However, because $MAPbI_3$ is ferroelastic, the presence of twin domains is expected, regardless of processing conditions. We also probed the entire film thickness (**Figure 1a**), but different types of twins, in particular TS1 vs. TS2, may predominantly exist near different interfaces. Bringing the perovskite closer to the cubic phase via either temperature or composition should lower the spontaneous strain, and thus reduce the size of the hysteresis loop.[18,86] In addition, dislocations at interfaces are known to pin domain walls, thus preventing domain wall movement.[87,88] Complete understanding of defect behavior in $MAPbI_3$-based devices will therefore likely require investigations of how grain size, temperature, pinning, substrate interface interactions and other parameters affect the ferroelastic hysteresis loop of $MAPbI_3$.

CONCLUSIONS

In conclusion, we have examined ferroelastic twinning in polycrystalline thin films of $MAPbI_3$. Strain inhomogeneity in films originated from specific twin domains. We then characterized the ferroelastic hysteresis loop of $MAPbI_3$, and identified approximate values for the onset of the loop (coercive stress) and saturation. External stress sources such as thermal stress from the substrate or roll-to-roll printing setups must apply at least |50| MPa to modify the proportions of different twins, and the temperature at which this occurs is substrate-dependent. Cyclic strain tests revealed changes to the unloading/reloading line locations in the stress-strain curve. Domains from differently-strained twin sets in the films are found to interact with each other, and convert from one twin set type to another. Degradation was found to correlate with domain wall presence, with more domain walls (*convex* bending) favoring degradation and fewer domain walls (*concave* bending) favoring stability. These results help to understand the structural processes related to defects in polycrystalline films of $MAPbI_3$, and the ionic and optoelectronic properties that they impact. We anticipate that the method presented above for characterizing the hysteresis loop will aid future studies of how strain and the hysteresis loop change under different device fabrication and operation conditions.

EXPERIMENTAL METHODS

Materials. Lead (II) iodide was purchased from Sigma Aldrich (PbI2 – 99.999% purity, trace metal basis) Methylammonium iodide (CH3NH3I, ≥ 99% purity) was purchased from Dyseol. N-N-dimethylformamide (DMF, 99.8%, anhydrous), dimethyl sulfoxide (DMSO, ≥ 99.9%, anhydrous), Chlorobenzene (99.8%, anhydrous) were purchased from Sigma Aldrich and kept in a nitrogen glove box.

Spin-casting of Kapton-PEDOT: PSS-MAPbI3-PMMA. Kapton sheets were cleaned via ultrasonication in isopropyl alcohol for 10 min. To stabilize the Kapton against further changes during heating, the cleaned sheets were carefully put between two aluminum plates, protected with very flat Al sheets, and the stack was heated at ≈ 350°C for 2h on a hot plate in an N2-filled glove box. Following this, the heat was turned off and the stack was allowed to cool naturally to room temperature. The pre-treated Kapton sheets were then exposed to an oxygen plasma at ~ 300 mTorr for 10 min, with air as the oxygen source. To keep the Kapton flat during spin-casting, the Kapton sheets were gently placed onto a glass slide covered with a thin PDMS sheet (for information on making the PDMS sheet, see reference 1). For annealing, the Kapton sheets were then removed from the glass-PDMS support. Care was taken to not bend the Kapton sheets during any of these steps. PEDOT: PSS (≈ 300 μL) was spin-cast in air onto the treated Kapton substrates at 2000 rpm for 10 seconds. The Kapton-PEDOT: PSS stack was annealed at 130°C for 4 min. To ensure film smoothness, 1) Kapton substrates of at least 2 cm × 2 cm size were required and 2) the PEDOT: PSS spin-casting and annealing procedures were repeated a second time, with the second annealing being 6 min. The samples were then transferred to a nitrogen-filled globe box for MAPbI3 and PMMA spin-casting. The precursor solution for MAPbI3 was fabricated in a nitrogen-filled glove box. PbI2 and CH3NH3I were dissolved in 1 mL DMF and 96 μL DMSO to make a 1M solution, and the mixture was stirred overnight under mild heating (60°C). The solution was then spin-cast onto the Kapton-PEDOT: PSS at 1000 rpm for 10 s then 4000 rpm for 30 s. When 8 s passed after the spin turned to 4000 rpm, 0.2 mL of anhydrous chlorobenzene was dropped on the substrate (23 seconds before the end of the coating). The films were then immediately annealed at 100 °C for 10 min on a hot plate, again in a nitrogen-filled glove box. All temperatures were verified with a thermocouple. PMMA was then cast onto the Kapton-PEDOT: PSS-MAPbI3 as a capping layer. 60 μL of a 25 mg/mL solution of PMMA in toluene was spin-cast onto the stack at 2000 rpm for 30 seconds, and no further annealing treatment was performed.

GIWAXS characterization. Grazing Incidence Wide-Angle X-Ray Scattering (GIWAXS) experiments were performed on beamline 11-3 (12.7 keV, wiggler side-station) at the Stanford Synchrotron Radiation Lightsource (SSRL). The source-to-detector (two-dimensional Rayonix MX225 CCD) distances were calibrated using lanthanum hexaboride (LaB6). All raw images were geometrically corrected using Nika. Sections (cakeslices) of the 2D GIWAXS patterns at specific angles were selected and integrated to obtain 1D patterns. GIWAXS analysis was performed primarily on two cakeslices: the first near-out-of-plane ("nOP", 18°-23° - Figure 1c) and the second near-in-plane ("nIP", 67°-72°). Both cakeslices were chosen to be 18° from 0° and 90°. Due to sample roughness and to avoid double diffraction issues, a large incidence angle (2°) was chosen, resulting in the entire MAPbI3 film thickness being probed, and the near-0° angles being cut off. Nevertheless, the parameters chosen enabled clear determination of near-in-plane vs. near-out-of-plane twin orientations and of the strain magnitudes of the planes in each domain. All patterns were converted to d from q, and all peaks were fit to Pseudo-Voigt patterns using Igor, with Gaussian and Lorentzian contributions kept constant (Igor Multipeak "shape" factor of 1) across all peaks and samples. The *d*-spacings of the peaks in Figure 3a were then compared with measured d-spacings of MAPbI3 single crystals at 300°K 2 to assign (220) vs. (004) nature and to calculate strain magnitude (see also discussion of Figures 3 and S3).

Other characterizations. Scanning Electron Microscopy was performed using an FEI Nova Nano 650 FEG SEM operating at 10-20 keV accelerating voltage with beam currents of 0.40-0.80 nA. For SEM measurements, the samples were sputter-coated with gold to prevent charging. No PMMA was cast on samples used for top-down measurements, to get accurate grain size measurements. Powder X-Ray Diffraction patterns were obtained using a Panalytical Empyrean powder diffractometer in reflection mode with a Cu-Kα source, operating with an accelerating voltage of 45 kV and beam current of 40 mA.

ASSOCIATED CONTENT

Supporting Information. Additional characterizations including Scanning Electron Microscopy (SEM), reproduction of certain experiments for 4 samples, further GIWAXS and XRD characterizations and analyses, as well as derivations and explanation of corrections applied. This material is available free of charge via the Internet at http://pubs.acs.org. (PDF)

AUTHOR INFORMATION

Corresponding Author

*Michael L. Chabinyc: mchabinyc@engineering.ucsb.edu

Author Contributions

The manuscript was written through contributions of all authors. All authors have given approval to the final version of the manuscript. The authors declare no competing financial interest.

ACKNOWLEDGMENT

Growth and structural characterization were supported by the U.S. Department of Energy, Office of Science, Basic Energy Sciences, under Award Number DE-SC-0012541. Support of optical characterization was provided by the U.S. Department of Energy (DOE), Office of Science, Basic Energy Sciences (BES), under Award Number DE-SC0019273. Use of the Stanford Synchrotron Radiation Lightsource, SLAC National Accelerator Laboratory, is supported by the U.S. Department of Energy, Office of Science, Office of Basic Energy Sciences under Contract No. DE-AC02-76SF00515. The research reported here also made use the shared facilities of the UCSB MRSEC (National Science Foundation DMR 1720256), a member of the Materials Research Facilities Network (www.mrfn.org). R.M.K. gratefully acknowledges the National Defense Science and Engineering Graduate fellowship for financial support. The authors would like to thank Prof. Anton Van der Ven for advice on ferroelasticity.

ABBREVIATIONS

GIWAXS, Grazing Incidence Wide-Angle X-Ray Scattering; f, fraction (by volume) of the film with a particular orientation; nIP, near-in-plane; nOP, near-out-of-plane.

REFERENCES

(1) Saliba, M.; Correa-Baena, J. P.; Wolff, C. M.; Stolterfoht, M.; Phung, N.; Albrecht, S.; Neher, D.; Abate, A. How to Make over 20% Efficient Perovskite Solar Cells in Regular (n-i-p) and Inverted (p-i-n) Architectures. *Chem. Mater.* **2018**, *30* (13), 4193-4201.

(2) National Renewable Energy Laboratory (NREL). Best Research Cell Efficiency Chart. https://www.nrel.gov/pv/cell-efficiency.html (accessed 2020-08-12).

(3) Mao, L.; Stoumpos, C. C.; Kanatzidis, M. G. Two-Dimensional Hybrid Halide Perovskites: Principles and Promises. *J. Am. Chem. Soc.* **2019**, *141* (3), 1171-1190.

(4) Zhang, T.; Yang, M.; Benson, E. E.; Li, Z.; Van De Lagemaat, J.; Luther, J. M.; Yan, Y.; Zhu, K.; Zhao, Y. A Facile Solvothermal Growth of Single Crystal Mixed Halide Perovskite $CH_3NH_3Pb(Br_{1-x}Cl_x)_3$. *Chem. Commun.* **2015**, *51* (37), 7820-7823.

(5) Kulkarni, S. A.; Baikie, T.; Boix, P. P.; Yantara, N.; Mathews, N.; Mhaisalkar, S. Band-Gap Tuning of Lead Halide Perovskites Using a Sequential Deposition Process. *J. Mater. Chem. A* **2014**, *2* (24), 9221-9225.

(6) Protesescu, L.; Yakunin, S.; Bodnarchuk, M. I.; Krieg, F.; Caputo, R.; Hendon, C. H.; Yang, R. X.; Walsh, A.; Kovalenko, M. V. Nanocrystals of Cesium Lead Halide Perovskites ($CsPbX_3$, X = Cl, Br, and I): Novel Optoelectronic Materials Showing Bright Emission with Wide Color Gamut. *Nano Lett.* **2015**, *15* (6), 3692-3696.

(7) Kennard, R. M.; Dahlman, C. J.; Nakayama, H.; Decrescent, R. A.; Schuller, J. A.; Seshadri, R.; Mukherjee, K.; Chabinyc, M. L. Phase Stability and Diffusion in Lateral Heterostructures of Methyl Ammonium Lead Halide Perovskites. *ACS Appl. Mater.*

Interfaces **2019**, *11* (28), 25313-25321.

(8) Venkatesan, N. R.; Kennard, R. M.; DeCrescent, R. A.; Nakayama, H.; Dahlman, C. J.; Perry, E. E.; Schuller, J.; Chabinyc, M. L. Phase Intergrowth and Structural Defects in Organic Metal Halide Ruddlesden-Popper Thin Films. *Chem. Mater.* **2018**, *30*, 8615-8623.

(9) Venkatesan, N. R.; Mahdi, A.; Barraza, B.; Wu, G.; Chabinyc, M. L.; Seshadri, R. Enhanced Yield-Mobility Products in Hybrid Halide Ruddlesden-Popper Compounds with Aromatic Ammonium Spacers. *Dalt. Trans.* **2019**, *48* (37), 14019-14026.

(10) Stoumpos, C. C.; Cao, D. H.; Clark, D. J.; Young, J.; Rondinelli, J. M.; Jang, J. I.; Hupp, J. T.; Kanatzidis, M. G. Ruddlesden-Popper Hybrid Lead Iodide Perovskite 2D Homologous Semiconductors. *Chem. Mater.* **2016**, *28* (8), 2852-2867.

(11) Jung, Y. S.; Hwang, K.; Heo, Y. J.; Kim, J. E.; Vak, D.; Kim, D. Y. Progress in Scalable Coating and Roll-to-Roll Compatible Printing Processes of Perovskite Solar Cells toward Realization of Commercialization. *Adv. Opt. Mater.* **2018**, *6* (9), 1-30.

(12) Jones, T. W.; Osherov, A.; Alsari, M.; Sponseller, M.; Duck, B. C.; Jung, Y. K.; Settens, C.; Niroui, F.; Brenes, R.; Stan, C. V.; et al. Lattice Strain Causes Non-Radiative Losses in Halide Perovskites. *Energy Environ. Sci.* **2019**, *12* (2), 596-606.

(13) Zhao, J.; Deng, Y.; Wei, H.; Zheng, X.; Yu, Z.; Shao, Y.; Shield, J. E.; Huang, J. Strained Hybrid Perovskite Thin Films and Their Impact on the Intrinsic Stability of Perovskite Solar Cells. *Sci. Adv.* **2017**, *3* (11).

(14) Rolston, N.; Bush, K. A.; Printz, A. D.; Gold-Parker, A.; Ding, Y.; Toney, M. F.; McGehee, M. D.; Dauskardt, R. H. Engineering Stress in Perovskite Solar Cells to Improve Stability.

Adv. Energy Mater. **2018**, *8* (29), 1-7.

(15) Wang, C.; Ma, L.; Guo, D.; Zhao, X.; Zhou, Z.; Lin, D.; Zhang, F.; Zhao, W.; Zhang, J.; Nie, Z. Balanced Strain-Dependent Carrier Dynamics in Flexible Organic-Inorganic Hybrid Perovskites. *J. Mater. Chem. C* **2020**, *8* (10), 3374-3379.

(16) Aizu, K. Determination of the State Parameters and Formulation of Spontaneous Strain for Ferroelastics. *Journal of the Physical Society of Japan*. 1970, pp 706-716.

(17) Aizu, K. Possible Species of Ferromagnetic, Ferroelectric, and Ferroelastic Crystals. *Phys. Rev. B* **1970**, *2* (3), 754-772.

(18) Salje, E. K. H. Mesoscopic Twin Patterns in Ferroelastic and Co-Elastic Minerals. *Rev. Mineral. Geochemistry* **2000**, *39* (1), 65-84.

(19) Wadhawan, V. K. Ferroelasticity. *Bull. Mater. Sci.* **1984**, *6* (4), 733-753.

(20) Baither, D.; Bartsch, M.; Baufeld, B.; Tikhonovsky, A.; Foitzik, A.; Rühle, M.; Messerschmidt, U. Ferroelastic and Plastic Deformation of T′-Zirconia Single Crystals. *J. Am. Ceram. Soc.* **2004**, *84* (8), 1755-1762.

(21) Chen, Y.; Xu, J.; Xie, S.; Nie, R.; Yuan, J.; Wang, Q.; Zhu, J. Failure Mode, Ferroelastic Behavior and Toughening Effect of Bismuth Titanate Ferroelectric Ceramics under Uniaxial Compression Load. *Mater. Des.* **2018**, *152*, 54-64.

(22) Araki, W.; Malzbender, J. Ferroelastic Deformation of $La_{0.58}Sr_{0.4}Co_{0.2}Fe_{0.8}O_{3-\delta}$ under Uniaxial Compressive Loading. *J. Eur. Ceram. Soc.* **2013**, *33* (4), 805-812.

(23) Pham, H. T.; Duong, T.; Weber, K. J.; Wong-Leung, J. Insights into Twinning Formation

in Cubic and Tetragonal Multi-Cation Mixed-Halide Perovskite. *ACS Mater. Lett.* **2020**, *2* (4), 415-424.

(24) Rothmann, M. U.; Li, W.; Zhu, Y.; Bach, U.; Spiccia, L.; Etheridge, J.; Cheng, Y. B. Direct Observation of Intrinsic Twin Domains in Tetragonal $CH_3NH_3PbI_3$. *Nat. Commun.* **2017**, *8*, 6-13.

(25) Hermes, I. M.; Bretschneider, S. A.; Bergmann, V. W.; Li, D.; Klasen, A.; Mars, J.; Tremel, W.; Laquai, F.; Butt, H. J.; Mezger, M.; et al. Ferroelastic Fingerprints in Methylammonium Lead Iodide Perovskite. *J. Phys. Chem. C* **2016**, *120* (10), 5724-5731.

(26) Wojciechowska, M.; Gagor, A.; Piecha-Bisiorek, A.; Jakubas, R.; Cizman, A.; Zaręba, J. K.; Nyk, M.; Zieliński, P.; Medycki, W.; Bil, A. Ferroelectricity and Ferroelasticity in Organic Inorganic Hybrid (Pyrrolidinium)$_3$[Sb_2Cl_9]. *Chem. Mater.* **2018**, *30* (14), 4597-4608.

(27) Huang, Y.; Yang, J.; Li, Z. J.; Qian, K.; Sao, F. High-Temperature Ferroelastic Phase Transition in a Perovskite-like Complex: $[Et_4N]_2[PbBr_3]_2$. *RSC Adv.* **2019**, *9* (18), 10364-10370.

(28) Chabin, M.; Gilletta, F. Experiment Investigation of the Ferroelastic Domain Structure in Cesium Lead Chloride in the Monoclinic Phase. *J. Appl. Crystallogr.* **1980**, *13* (6), 539-543.

(29) Huang, B.; Kong, G.; Esfahani, E. N.; Chen, S.; Li, Q.; Yu, J.; Xu, N.; Zhang, Y.; Xie, S.; Wen, H.; et al. Ferroic Domains Regulate Photocurrent in Single-Crystalline $CH_3NH_3PbI_3$ Films Self-Grown on FTO/TiO_2 Substrate. *npj Quantum Mater.* **2018**, *3* (1), 1-8.

(30) Strelcov, E.; Dong, Q.; Li, T.; Chae, J.; Shao, Y.; Deng, Y.; Gruverman, A.; Huang, J.; Centrone, A. $CH_3NH_3PbI_3$ Perovskites: Ferroelasticity Revealed. *Sci. Adv.* **2017**, *3* (4), e1602165.

(31) Medjahed, A. A.; Dally, P.; Zhou, T.; Lemaitre, N.; Djurado, D.; Reiss, P.; Pouget, S. Unraveling the Formation Mechanism and Ferroelastic Behavior of $MAPbI_3$ Perovskite Thin Films Prepared in the Presence of Chloride . *Chem. Mater.* **2020**, *32* (8), 3346-3357.

(32) Wilson, J. N.; Frost, J. M.; Wallace, S. K.; Walsh, A. Dielectric and Ferroic Properties of Metal Halide Perovskites. *APL Mater.* **2019**, *7* (1), 010901.

(33) Minkiewicz, V. J.; Shirane, G. Soft Phonon Modes in $KMnF_3$. *J. Phys. Soc. Japan* **1969**, *26* (3), 674-680.

(34) Axe, J. D.; Shirane, G.; Müller, K. A. Zone-Boundary Phonon Instability in Cubic $LaAlO_3$. *Phys. Rev.* **1969**, *183* (3), 820-823.

(35) Shirane, G.; Yamada, Y. Lattice-Dynamical Study of the 110Â°K Phase Transition in $SrTiO_3$. *Phys. Rev.* **1969**, *177* (2), 858-863.

(36) Sakashita, H.; Ohama, N.; Okazaki, A. Thermal Expansion and Spontaneous Strain of $KMnF_3$ near the 186 K-Structural Phase Transition. *Phase Transitions* **1990**, *28* (1-4), 99-106.

(37) Whitfield, P. S.; Herron, N.; Guise, W. E.; Page, K.; Cheng, Y. Q.; Milas, I.; Crawford, M. K. Structures, Phase Transitions and Tricritical Behavior of the Hybrid Perovskite Methyl Ammonium Lead Iodide. *Sci. Rep.* **2016**, *6* (June), 1-16.

(38) Poglitsch, A.; Weber, D. Dynamic Disorder in Methylammoniumtrihalogenoplumbates (II)

Observed by Millimeter-Wave Spectroscopy. *J. Chem. Phys.* **1987**, *87* (11), 6373-6378.

(39) Baikie, T.; Fang, Y.; Kadro, J. M.; Schreyer, M.; Wei, F.; Mhaisalkar, S. G.; Graetzel, M.; White, T. J. Synthesis and Crystal Chemistry of the Hybrid Perovskite $(CH_3NH_3)PbI_3$ for Solid-State Sensitised Solar Cell Applications. *J. Mater. Chem. A* **2013**, *1* (18), 5628-5641.

(40) Fang, H. H.; Raissa, R.; Abdu-Aguye, M.; Adjokatse, S.; Blake, G. R.; Even, J.; Loi, M. A. Photophysics of Organic-Inorganic Hybrid Lead Iodide Perovskite Single Crystals. *Adv. Funct. Mater.* **2015**, *25* (16), 2378-2385.

(41) Weller, M. T.; Weber, O. J.; Henry, P. F.; Di Pumpo, A. M.; Hansen, T. C. Complete Structure and Cation Orientation in the Perovskite Photovoltaic Methylammonium Lead Iodide between 100 and 352 K. *Chem. Commun.* **2015**, *51* (20), 4180-4183.

(42) Kawamura, Y.; Mashiyama, H.; Hasebe, K. Structural Study on Cubic-Tetragonal Transition of $CH_3NH_3PbI_3$. *J. Phys. Soc. Japan* **2002**, *71* (7), 1694-1697.

(43) Hermes, I. M.; Best, A.; Winkelmann, L.; Mars, J.; Vorpahl, S. M.; Mezger, M.; Collins, L.; Butt, H.-J.; Ginger, D. S.; Koynov, K.; et al. Anisotropic Carrier Diffusion in Single $MAPbI_3$ Grains Correlates to Their Twin Domains . *Energy Environ. Sci.* **2020**, *13*, 4168-4177.

(44) Shi, R.; Zhang, Z.; Fang, W. H.; Long, R. Ferroelastic Domains Drive Charge Separation and Suppress Electron-Hole Recombination in All-Inorganic Halide Perovskites: Time-Domain: Ab Initio Analysis. *Nanoscale Horizons* **2020**, *5* (4), 683-690.

(45) Warwick, A. R.; Íniguez, J.; Haynes, P. D.; Bristowe, N. C. First-Principles Study of Ferroelastic Twins in Halide Perovskites. *J. Phys. Chem. Lett.* **2019**, *10* (6), 1416-1421.

(46) Lim, A. R.; Jeong, S. Y. Twin Structure by 133Cs NMR in Ferroelastic $CsPbCl_3$ Crystal. *Solid State Commun.* **1999**, *110* (3), 131-136.

(47) Bechtel, J. S.; Van Der Ven, A. Octahedral Tilting Instabilities in Inorganic Halide Perovskites. *Phys. Rev. Mater.* **2018**, *2* (2), 1-13.

(48) Bechtel, J. S.; Thomas, J. C.; Van Der Ven, A. Finite-Temperature Simulation of Anharmonicity and Octahedral Tilting Transitions in Halide Perovskites. *Phys. Rev. Mater.* **2019**, *3* (11), 1-10.

(49) Maughan, A. E.; Mozur, E. M.; Candia, A. M.; Neilson, J. R. Ferroelastic Phase Transition in Formamidinium Tin(IV) Iodide Driven by Organic-Inorganic Coupling. *Inorg. Chem.* **2020**, *59* (19), 14399-14406.

(50) He, X.; Li, S.; Ding, X.; Sun, J.; Selbach, S. M.; Salje, E. K. H. The Interaction between Vacancies and Twin Walls, Junctions, and Kinks, and Their Mechanical Properties in Ferroelastic Materials. *Acta Mater.* **2019**, *178*, 26-35.

(51) Farokhipoor, S.; Noheda, B. Local Conductivity and the Role of Vacancies around Twin Walls of (001)-$BiFeO_3$ Thin Films. *J. Appl. Phys.* **2012**, *112* (5).

(52) Aird, A.; Salje, E. K. H. Enhanced Reactivity of Domain Walls in WO_3 with Sodius. *Eur. Phys. J. B* **2000**, *15* (2), 205.

(53) Klie, R. F.; Ito, Y.; Stemmer, S.; Browning, N. D. Observation of Oxygen Vacancy Ordering and Segregation in Perovskite Oxides. *Ultramicroscopy* **2001**, *86* (3-4), 289-302.

(54) Reza, K. M.; Mabrouk, S.; Qiao, Q. A Review on Tailoring PEDOT:PSS Layer for Improved Performance of Perovskite Solar Cells. *Proc. Nat. Res. Soc.* **2018**, *2* (January).

(55) Sun, K.; Li, P.; Xia, Y.; Chang, J.; Ouyang, J. Transparent Conductive Oxide-Free Perovskite Solar Cells with PEDOT:PSS as Transparent Electrode. *ACS Appl. Mater. Interfaces* **2015**, *7* (28), 15314-15320.

(56) Chen, L. C.; Chen, C. C.; Chen, J. C.; Wu, C. G. Annealing Effects on High-Performance $CH_3NH_3PbI_3$ Perovskite Solar Cells Prepared by Solution-Process. *Sol. Energy* **2015**, *122*, 1047-1051.

(57) Ava, T. T.; Al Mamun, A.; Marsillac, S.; Namkoong, G. A Review: Thermal Stability of Methylammonium Lead Halide Based Perovskite Solar Cells. *Appl. Sci.* **2019**, *9* (1), 188.

(58) Jariwala, S.; Sun, H.; Adhyaksa, G. W. P.; Lof, A.; Muscarella, L. A.; Ehrler, B.; Garnett, E. C.; Ginger, D. S. Local Crystal Misorientation Influences Non-Radiative Recombination in Halide Perovskites. *Joule* **2019**, *3* (12), 3048-3060.

(59) Henke, B. L.; Gullikson, E. M.; Davis, J. C. X-Ray Interactions: Photoabsorption, Scattering, Transmission, and Reflection at E = 50-30, 000 EV, Z = 1-92. *Atomic Data and Nuclear Data Tables*. 1993, pp 181-342.

(60) GIXA Calculator for Penetration Depth (and Optical Properties) for X-rays https://gixa.ati.tuwien.ac.at/tools/penetrationdepth.xhtml (accessed Nov 9, 2020).

(61) Hu, Y. H.; Chan, H. M.; Wen, Z. X.; Harmer, M. P. Scanning Electron Microscopy and Transmission Electron Microscopy Study of Ferroelectric Domains in Doped $BaTiO_3$. *J. Am. Ceram. Soc.* **1986**, *69* (8), 594-602.

(62) Cheng, S. Y.; Ho, N. J.; Lu, H. Y. Transformation-Induced Twinning: The 90° and 180° Ferroelectric Domains in Tetragonal Barium Titanate. *J. Am. Ceram. Soc.* **2006**, *89* (7),

2177-2187.

(63) Feng, J. Mechanical Properties of Hybrid Organic-Inorganic $CH_3NH_3BX_3$ (B = Sn, Pb; X = Br, I) Perovskites for Solar Cell Absorbers. *APL Mater.* **2014**, *2* (8), 081801.

(64) Steele, J. A.; Jin, H.; Dovgaliuk, I.; Berger, R. F.; Braeckevelt, T.; Yuan, H.; Martin, C.; Solano, E.; Lejaeghere, K.; Rogge, S. M. J.; et al. Thermal Unequilibrium of Strained Black $CsPbI_3$ Thin Films. *Science (80-.).* **2019**, *365* (6454), 679-684.

(65) Spina, M.; Karimi, A.; Andreoni, W.; Pignedoli, C. A.; Náfrádi, B.; Forró, L.; Horváth, E. Mechanical Signatures of Degradation of the Photovoltaic Perovskite $CH_3NH_3PbI_3$ upon Water Vapor Exposure. *Appl. Phys. Lett.* **2017**, *110* (12). 121903.

(66) Rakita, Y.; Cohen, S. R.; Kedem, N. K.; Hodes, G.; Cahen, D. Mechanical Properties of $APbX_3$ (A = Cs or CH_3NH_3; X = I or Br) Perovskite Single Crystals. *MRS Commun.* **2015**, *5* (4), 623-629.

(67) Sun, S.; Fang, Y.; Kieslich, G.; White, T. J.; Cheetham, A. K. Mechanical Properties of Organic-Inorganic Halide Perovskites, $CH_3NH_3PbX_3$ (X = I, Br and Cl), by Nanoindentation. *J. Mater. Chem. A* **2015**, *3* (36), 18450-18455.

(68) Jacobsson, T. J.; Schwan, L. J.; Ottosson, M.; Hagfeldt, A.; Edvinsson, T. Determination of Thermal Expansion Coefficients and Locating the Temperature-Induced Phase Transition in Methylammonium Lead Perovskites Using X-Ray Diffraction. *Inorg. Chem.* **2015**, *54* (22), 10678-10685.

(69) Ramirez, C.; Yadavalli, S. K.; Garces, H. F.; Zhou, Y.; Padture, N. P. Thermo-Mechanical Behavior of Organic-Inorganic Halide Perovskites for Solar Cells. *Scr. Mater.* **2018**, *150*,

36-41.

(70) Elsner, G.; Kempf, J.; Bartha, J. W.; Wagner, H. H. Anisotropy of Thermal Expansion of Thin Polyimide Films. *Thin Solid Films* **1990**, *185*, 189-197.

(71) Polyimide (PI) Material Information, Thermal Properties http://www.goodfellow.com/E/Polyimide.html (accessed Jul 7, 2020).

(72) Music, D.; Elalfy, L. Tuneable Thermal Expansion of Poly (3,4-Ethylenedioxythiophene) Polystyrene Sulfonate. *J. Phys. Condens. Matter* **2019**, *31* (12), 125101.

(73) Tangram Technology Ltd. 2000. Polymer Data File: Polymethyl Methacrylate - PMMA (Acrylic). http://www.tangram.co.uk/TI-Polymer-PMMA.html (Last edited: 20/05/15; accessed 2020-08-20).

(74) Salje, E. K. *Phase Transitions in Ferroelastic and Co-Elastic Crystals,* Cambridge University Press, 1993, 1-12.

(75) Thomas, J. C.; Van Der Ven, A. Order Parameters for Symmetry-Breaking Structural Transitions: The Tetragonal-Monoclinic Transition in ZrO_2. *Phys. Rev. B* **2017**, *96* (13), 1-13.

(76) Ahn, S. M.; Jung, E. D.; Kim, S. H.; Kim, H.; Lee, S.; Song, M. H.; Kim, J. Y. Nanomechanical Approach for Flexibility of Organic-Inorganic Hybrid Perovskite Solar Cells. *Nano Lett.* **2019**, *19* (6), 3707-3715.

(77) Suo, Z.; Ma, E. Y.; Gleskova, H.; Wagner, S. Mechanics of Rollable and Foldable Film-on-Foil Electronics. *Appl. Phys. Lett.* **1999**, *74* (8), 1177-1179.

(78) Wang, Y.; Chen, Z.; Deschler, F.; Sun, X.; Lu, T. M.; Wertz, E. A.; Hu, J. M.; Shi, J. Epitaxial Halide Perovskite Lateral Double Heterostructure. *ACS Nano* **2017**, *11* (3), 3355-3364.

(79) Okuzaki, H.; Ishihara, M. Spinning and Characterization of Conducting Microfibers. *Macromol. Rapid Commun.* **2003**, *24* (3), 261-264.

(80) Bush, K. A.; Rolston, N.; Gold-Parker, A.; Manzoor, S.; Hausele, J.; Yu, Z. J.; Raiford, J. A.; Cheacharoen, R.; Holman, Z. C.; Toney, M. F.; et al. Controlling Thin-Film Stress and Wrinkling during Perovskite Film Formation. *ACS Energy Lett.* **2018**, *3* (6), 1225-1232.

(81) He, X.; Salje, E. K. H.; Ding, X.; Sun, J. Immobile Defects in Ferroelastic Walls: Wall Nucleation at Defect Sites. *Appl. Phys. Lett.* **2018**, *112* (9), 2-6.

(82) Salje, E. K. H.; Hayward, S. A.; Lee, W. T. Ferroelastic Phase Transitions: Structure and Microstructure. *Acta Crystallogr. Sect. A Found. Crystallogr.* **2005**, *61* (1), 3-18.

(83) Xu, H.; Heaney, P. J. Memory Effects of Domain Structures during Displacive Phase Transitions: A High-Temperature TEM Study of Quartz and Anorthite. *Am. Mineral.* **1997**, *82* (1-2), 99-108.

(84) Arlt, G. Twinning in Ferroelectric and Ferroelastic Ceramics: Stress Relief. *J. Mater. Sci.* **1990**, *25* (6), 2655-2666.

(85) DeQuilettes, D. W.; Vorpahl, S. M.; Stranks, S. D.; Nagaoka, H.; Eperon, G. E.; Ziffer, M. E.; Snaith, H. J.; Ginger, D. S. Impact of Microstructure on Local Carrier Lifetime in Perovskite Solar Cells. *Science (80-.).* **2015**, *348* (6235), 683-686.

(86) Yu, Y. S.; Jang, M. S.; Kim, H. J.; Cho, C. R. A Study on the Twin Domain of $Pb_3(PO_4)_2$

Ferroelastic Crystal. *Ferroelectrics* **1993**, *142* (1), 121-130.

(87) Chu, M. W.; Szafraniak, I.; Hesse, D.; Alexe, M.; Gösele, U. Elastic Coupling between 90° Twin Walls and Interfacial Dislocations in Epitaxial Ferroelectric Perovskites: A Quantitative High-Resolution Transmission Electron Microscopy Study. *Phys. Rev. B - Condens. Matter Mater. Phys.* **2005**, *72* (17), 1-5.

(88) Su, D.; Meng, Q.; Vaz, C. A. F.; Han, M. G.; Segal, Y.; Walker, F. J.; Sawicki, M.; Broadbridge, C.; Ahn, C. H. Origin of 90° Domain Wall Pinning in $Pb(Zr_{0.2}Ti_{0.8})O_3$ Heteroepitaxial Thin Films. *Appl. Phys. Lett.* **2011**, *99* (10), 8-11.

TOC Figure

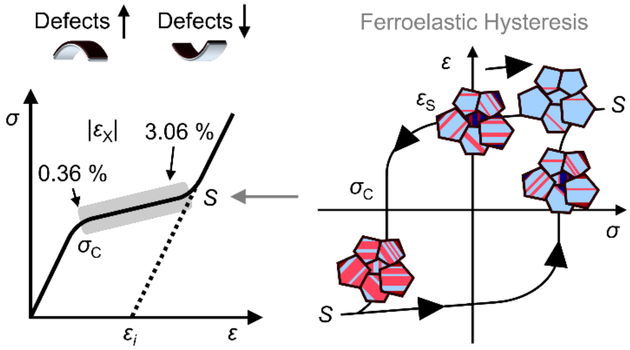
Defects ↑
Defects ↓
σ
|ε_X|
3.06 %
0.36 %
S
σ_C
ε_i
ε
Ferroelastic Hysteresis
ε
ε_S
S
σ_C
σ
S

Ferroelastic Hysteresis in Thin Films of Methylammonium Lead Iodide

Supporting Information

Rhys M. Kennard, [†] Clayton J. Dahlman, [†] Ryan A. DeCrescent, [‡] Jon A. Schuller, [‖] Kunal Mukherjee, [†] Ram Seshadri, [†+] Michael L. Chabinyc [†*]

† Materials Department, University of California, Santa Barbara, CA 93106, United States

‡ Department of Physics, University of California, Santa Barbara, CA 93106, United States

‖ Department of Electrical and Computer Engineering, University of California, Santa Barbara, CA 93106, United States

+Department of Chemistry and Biochemistry, University of California, Santa Barbara, CA 93106, United States

*Corresponding Author: mchabinyc@engineering.ucsb.edu

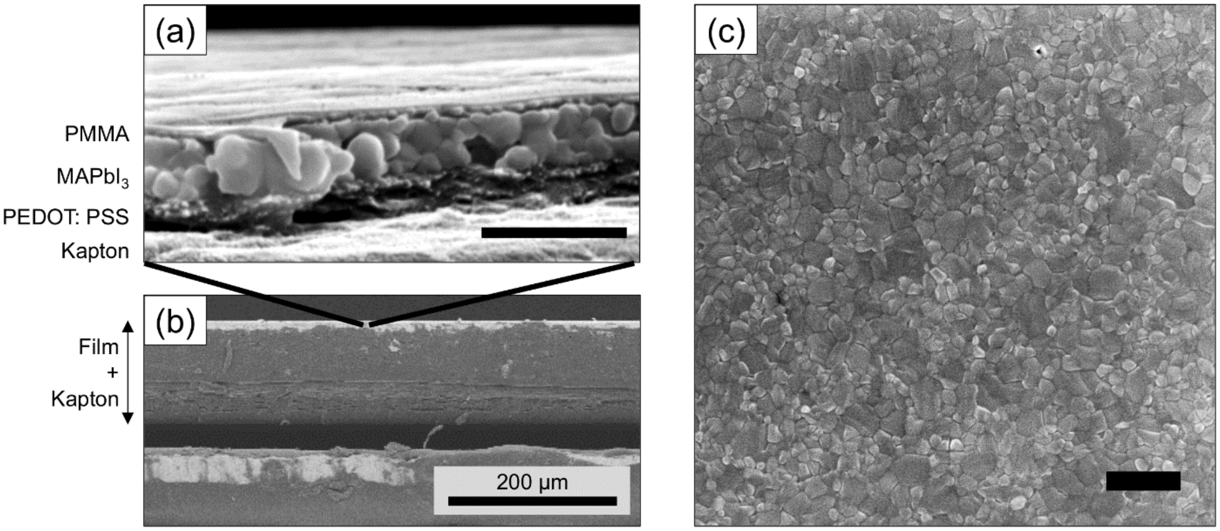

Figure S1. SEM images of an as-cast film, showing (a) a cross-section of an as-cast film, (b) a lower-magnification cross-section showing the Kapton thickness and (c) a top-view image of an $MAPbI_3$ film on top of which no PMMA was cast. 19 keV accelerating voltage was used for (a) and (c) and 10 keV was used for (b). Scale bars in (a) and (c) are 1 µm.

The $MAPbI_3$ film measured here was 1-4 grains thick. Because the films were cast on plastic substrates, they did not break in half cleanly, so parallax issues were encountered when trying to determine thickness. The exact thicknesses were difficult to measure, but were approximately 400 nm for $MAPbI_3$, 200 nm for PEDOT: PSS and 50 nm for PMMA. To properly measure grain size without parallax issues, we measured a film from the top (**FigureS1c**) that did not have PMMA. The average grain size was estimated from measurement of 100 grain widths to be 200 ± 100 nm.

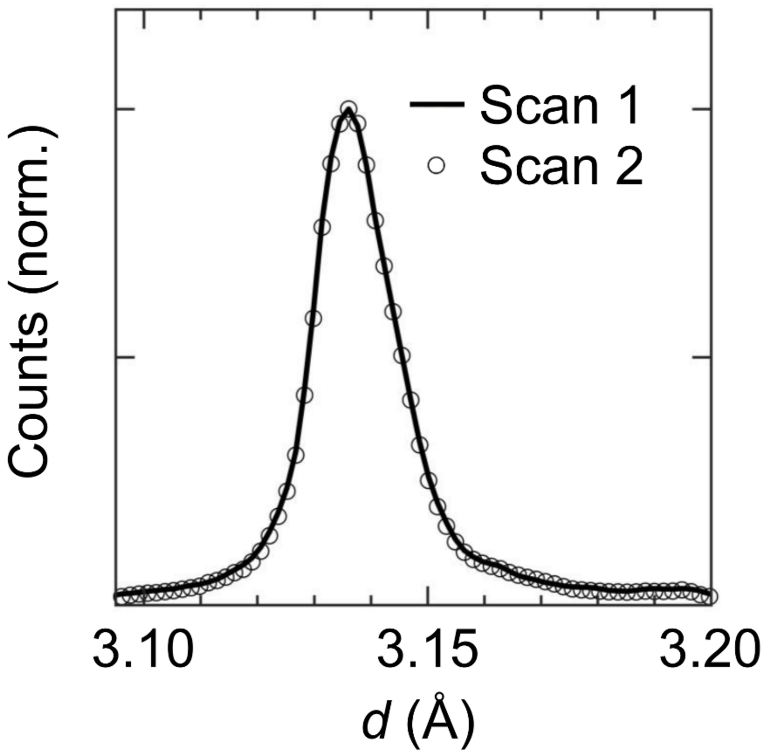

Figure S2. GIWAXS nOP patterns of films bent *concavely* around a cylinder with 4.1 mm diameter. Scan 1 and Scan 2 indicate two consecutive scans of the same sample, showing lack of change and thus good stability under the beam.

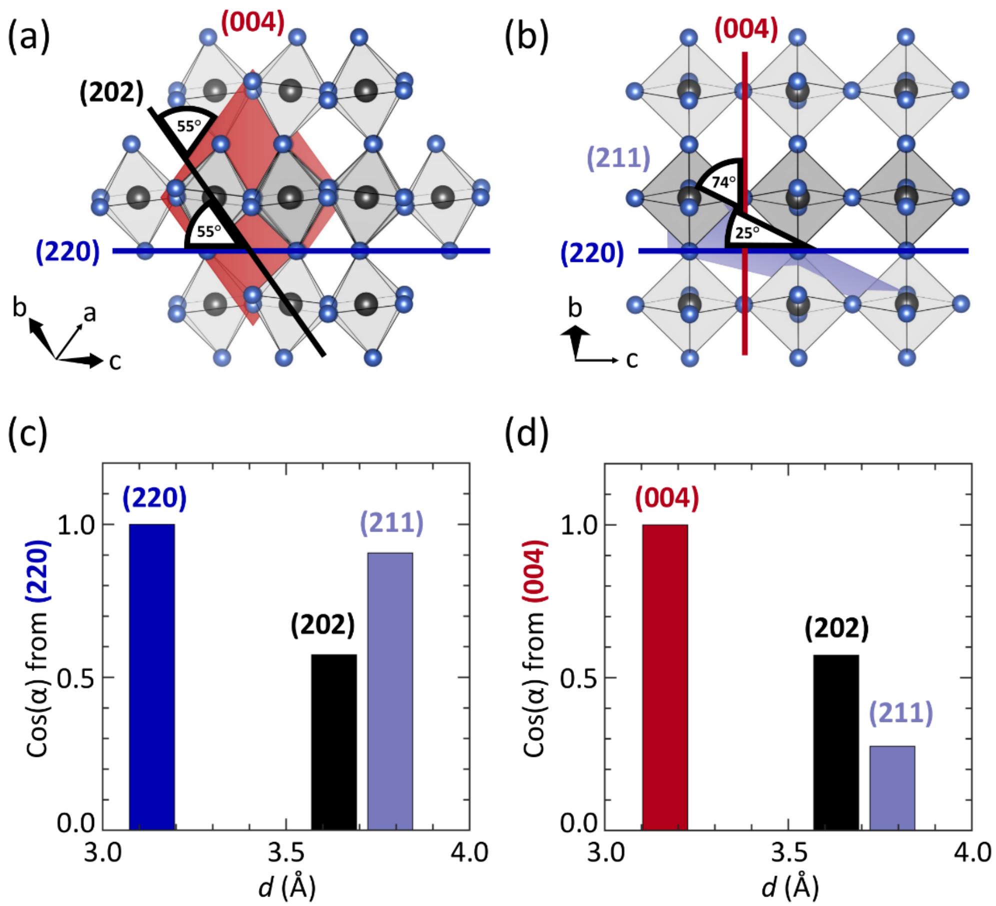

Figure S3. Crystal structures of $MAPbI_3$ in the tetragonal I4/mcm phase [2] showing (a) the angles made between the (202) plane and the (220) and (004) planes and (b) the angles made between the (211) plane and the (220) and (004) planes. (c-d) Cosines of the angles in (a) and (b) respectively.

In order to properly assign GIWAXS peaks as (220) vs. (004), we tracked the intensity of the (211) peak with respect to its neighboring (202) peak. **Figures S3a-b** show the angles that the (202) (**Figure S3a**) and (211) (**Figure S3b**) planes make with the (220) and (004) planes. Conveniently, the (202) plane is at equal angle from the (220) and (004), making normalization of the (211) with respect to the (202) useful for analysis (i.e. the (202) is a reference point and the (211) intensity will reveal (220) or (004) predominance). The cosines of the above-mentioned angles are shown in **Figure S3c-d**. Because the (211) plane is nearly parallel to the (220), much stronger (211) intensity will be observed when the peak at $d \approx 3.1$-3.2 Å is (220) (**Figure S3c**). Correspondingly, because the (211) is nearly perpendicular to the (004), a weak (211) intensity with respect to the neighboring (202) peak likely indicates that the peak at $d \approx 3.1$-3.2 Å is (004) (**Figure S3d**). So, in nOP patterns, strong (211) correlates more with A domains and weak (211) correlates more with C domains. To further verify these assignments, we compared the nOP patterns with the nIP patterns, as a domain with (220) reflections out-of-plane should have corresponding (004) reflections in-plane (**Figure 3**).

Additional information regarding fraction *f*

To calculate f, the fitted peak intensities were corrected for structure factor, [3,4] and we used **Equation 1**:

$$f = 100 \times \frac{I_{Corr,peak\ of\ interest}}{I_{Corr,total}} \qquad (1)$$

Where I_{Corr} is the corrected peak intensity.

f represents the fraction of the film having (220) or (004) reflections, in the nOP *or* the nIP patterns. Thus, it is important to correct the scattering intensities of (220) and (004) relative to each other. The intensities I_{hkl} of a peak (*hkl*) ((220) or (004)) were therefore corrected for structure factor F_{hkl}, using $I_{Corr} = (I_{\mathrm{hkl}})(F_{\mathrm{hkl}})^2$. [3] Conveniently, the (220) and (004) peaks were always within ≤ 0.1 Å of each other, and we calculated the fs for each *for the same nOP or nIP pattern*. Other correction factors [3] that might otherwise be necessary were therefore ignored, such as the Debye-Waller thermal correction or Lorentz/polarization factors. In addition, because each pattern probed specific domain orientations and not a powder sample, the multiplicity of all peaks should be 1. Thus, the corrected intensities were $I_{Corr} = (I_{\mathrm{hkl}})(F_{\mathrm{hkl}})^2$.

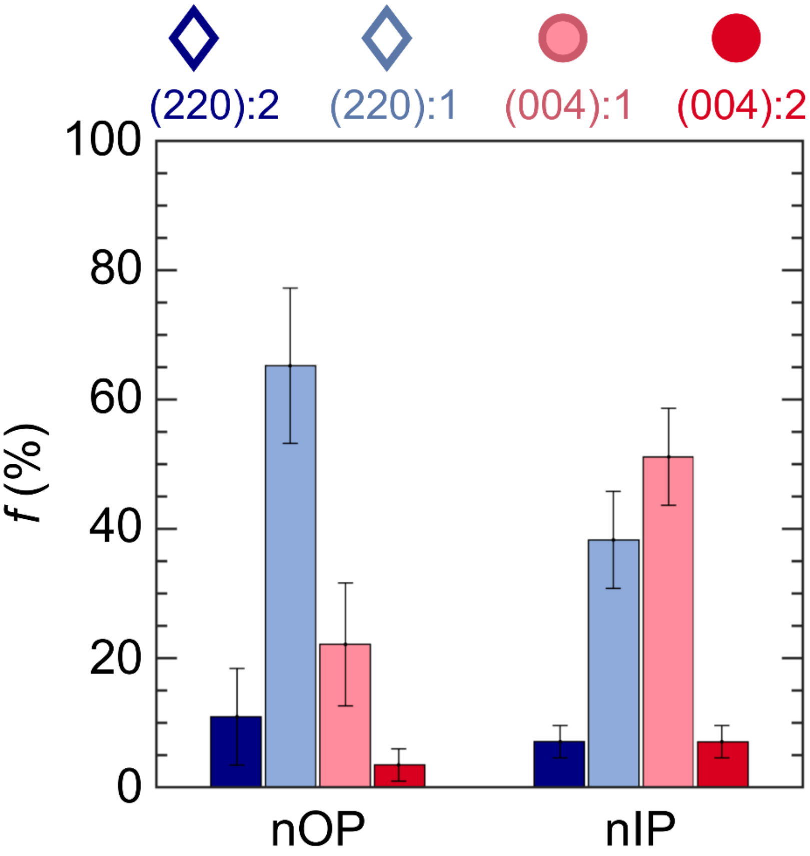

Figure S4. Reproduction of **Figure 3c** for 4 samples, where the values are the average *f*s and the error bars represent the standard deviation of these values. The results reproduce those shown in **Figure 3**, albeit with larger uncertainty values.

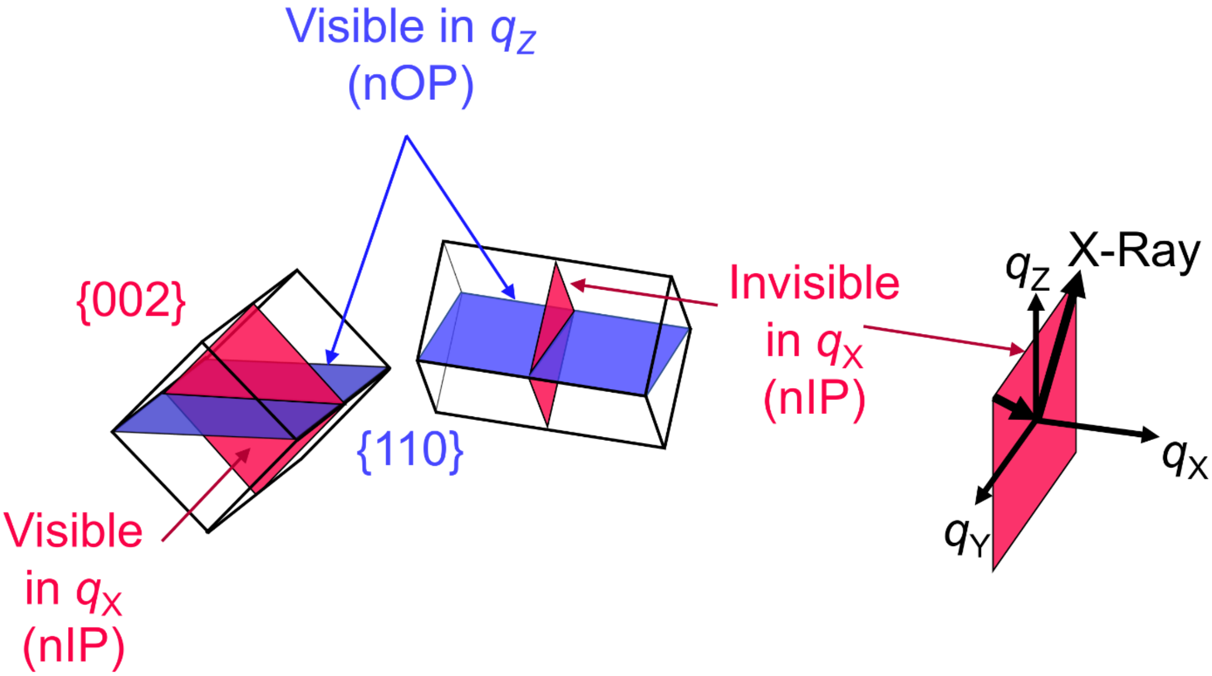

Figure S5. A-type domains with all planes visible nOP but with only some planes visible nIP, depending on domain rotation. Two A-type domains with the orientation shown here, and with a domain wall between them belonging to {112}, would exhibit 90° *a-a* type twinning (also possible in this study).

Derivation of Equation for Minimum Domain Size D_{min}

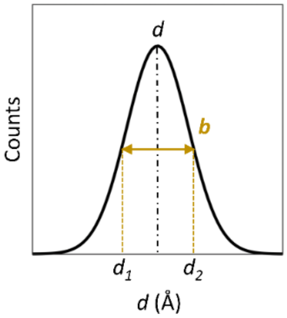

Figure S6. Sample peak in real-space, showing a peak of center d, with breadth b spanning from d_1 to d_2.

Here, we extracted peak breadths to obtain domain size. Because we did this only for one peak, rather than over a series of peaks, the numbers reported in this study should be taken as the *minimum* domain size. We did not calculate size from a series of peaks because the (110) and (002) peaks significantly overlapped with each other and because the (330) and (006) peaks significantly overlapped with substrate peaks, so the (220) and (004) peaks were best for breadth calculations. For this reason, we caution that the following analysis provides estimates only, because the effects of strain are not decoupled from peak width, over multiple peaks. We do note, however, that the results of this analysis (number of walls increases or decreases) are consistent with prior microscopy observations. [5] We were also primarily concerned with *relative changes* to D_{min} upon application of stress, not with the absolute values of the numbers themselves.

Prior work modified the Scherrer equation for GIWAXS to obtain the following: [6]

$$D_{hkl} = \frac{2\pi K}{\Delta q_{hkl}}$$

Where D_{hlk} is the average domain size, K is an *hkl*-dependent constant [7] and Δq_{hkl} is the breadth of the Bragg reflection *hkl* in reciprocal space. However, because we analyzed all our data in real-space (*d*-spacings) and not in reciprocal space (*q*), we converted the above equation to real-space. Because $q = 2\pi/d$ and $\Delta q_{hkl} = q_1 - q_2$:

$$\Delta q_{hkl} = 2\pi\left(\frac{1}{d_1} - \frac{1}{d_2}\right) = 2\pi\left(\frac{d_2 - d_1}{d_1 d_2}\right) = 2\pi\left(\frac{b}{d_1 d_2}\right)$$

Where b is the breadth (area divided by intensity)[6] in real space, d is the center of the *hkl* peak, $d_1 = d - b/2$ and $d_2 = d + b/2$ (see **Figure S6).** Thus,

$$\Delta q_{hkl} = 2\pi\left(\frac{b}{\left(d - {}^{b}/_{2}\right)\left(d + {}^{b}/_{2}\right)}\right) = 2\pi b\left(\frac{1}{d^2 - {}^{b^2}/_{4}}\right)$$

$$D_{min} = \frac{K}{b}\left(d^2 - {}^{b^2}/_{4}\right)$$

Where *K* is the Scherrer constant (≈ 1.0 for both (220) and (004)) [7], *b* is the breadth which in this case is the peak area divided by the peak intensity (uncorrected), and *d* is the *d*-spacing. Pseudo-Voigt fitting methodology was applied to all samples.

Calculation of Applied Strain Magnitudes

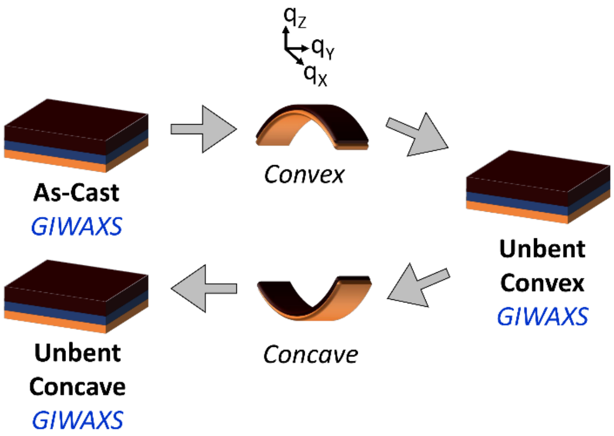

Figure S7. Bending experiment for convex and concave bending. GIWAXS patterns were taken after the applied strain was released.

Here we calculate the approximate magnitudes of the strains ε applied to $MAPbI_3$ films during bending (**Figure S7**). To do so, we use the equation provided by Suo *et al.*: [8]

$$\varepsilon_{top,\ qx} = \left(\frac{t_f + t_S}{2R}\right)\frac{(1 + 2\eta + \chi\eta^2)}{(1 + \eta)(1 + \chi\eta)}$$

In this equation, the "top" designates the top region of the Kapton-PEDOT: PSS-$MAPbI_3$-PMMA stack; thus, the area closest to $MAPbI_3$. "qx" designates the strain in the q_X direction; i.e. in-plane. R is the radius around which the film is bent (so $2R$ is the diameter), t_f is the film thickness, t_S is the substrate thickness, $\eta = t_f/t_S$ and χ is the ratio of elastic moduli Y, where $\chi = Y_f/Y_S$.

The Young's modulus of $MAPbI_3$ has been found to vary between 10 and 20 GPa (≈ 10, 12.8, 14, and 20 GPa); [9–12] so we take 14 GPa here as a mid-range value for approximation. The moduli of PEDOT: PSS is ≈ 2 GPa [13], that of PMMA is 3 GPa and that of Kapton is 2.5 GPa. Because the moduli of PEDOT: PSS and Kapton are not only very similar but also an order of magnitude lower than that of $MAPbI_3$, we can approximate the "substrate" as being composed of Kapton and PEDOT: PSS. In addition, because the modulus of PMMA is much lower than that of $MAPbI_3$ and because the PMMA layer is much thinner than the $MAPbI_3$ layer, we can approximate the "film" as being $MAPbI_3$ only. Thus, $\chi = Y_f/Y_S \approx Y_{MAPbI3}/Y_{Kapton} \approx$ (14 GPa) / (2.5 GPa) ≈ 5.6.

Next, from **Figure S1**, we obtained the thickness of Kapton t_{Kapton} (125 000 nm), of PEDOT: PSS (≈ 200 nm), of $MAPbI_3$ (≈ 400 nm) and of PMMA (≈ 50 nm). Assuming again that the "substrate" is Kapton + PEDOT: PSS and that the "film" is $MAPbI_3$, $\eta = t_f/t_S \approx$ (400 nm)/(125200 nm) ≈ 0.00319. Because $\eta \sim 10^{-3}$, $\varepsilon_{top,\ qx}$ is practically independent of both η and χ.[8] We can therefore approximate the applied strain in the q_X direction:

$$\varepsilon_X \approx \left(\frac{t_f + t_S}{2R}\right)$$

The ε_X obtained are listed in **Table 1**. Then, Poisson's ratio was used to calculate ε_Z.

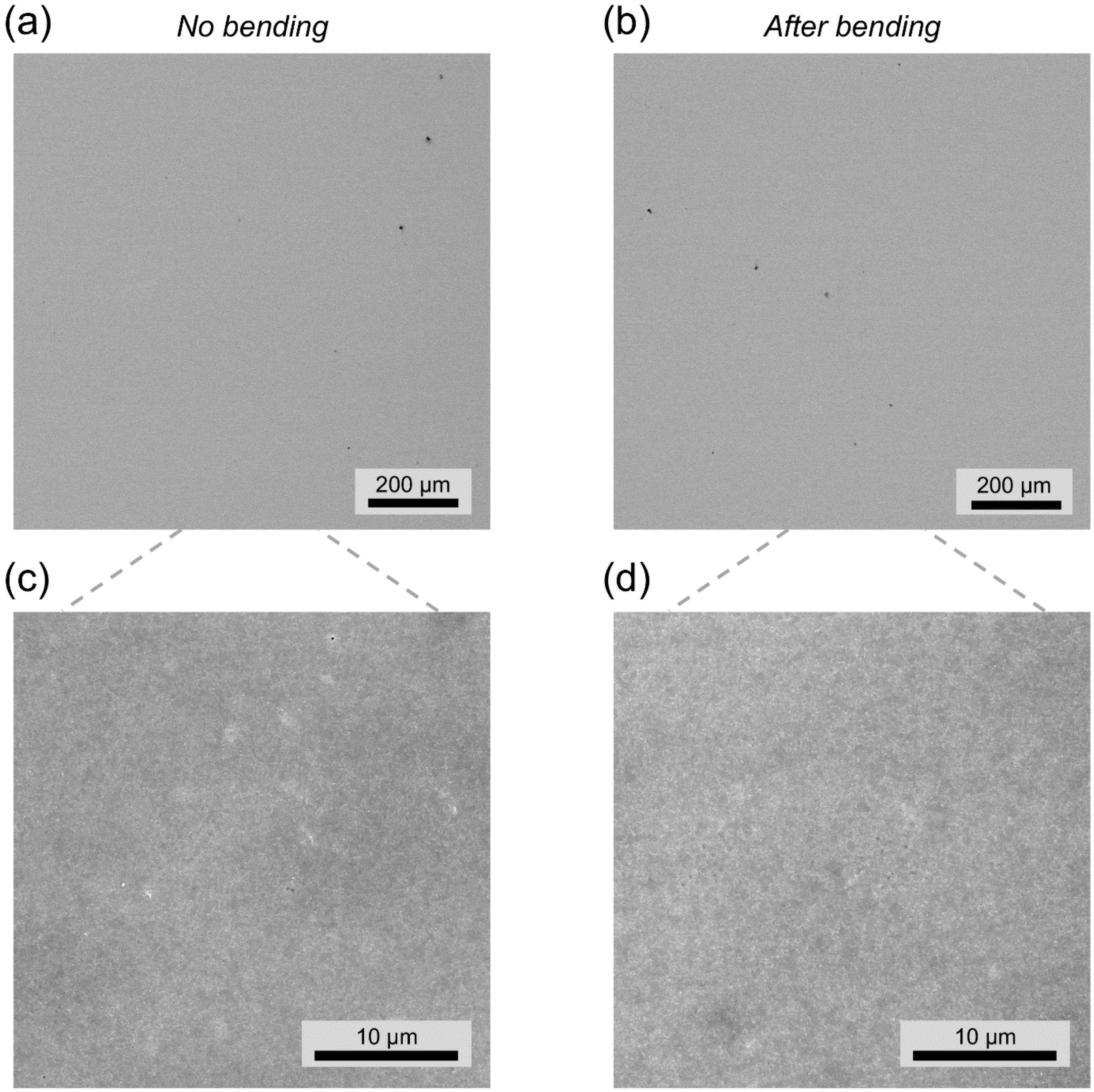

Figure S8. SEM micrographs of films with no bending ((a), (c)) and after bending 2 times ((b), (d)) *convexly* around a diameter of 4.1 mm, with low and high magnifications. No cracks were observed here. (19 keV)

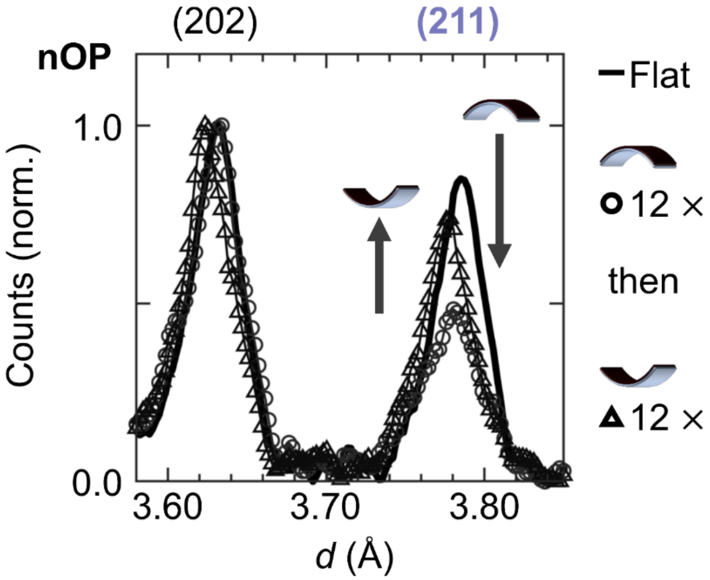

Figure S9. (211)-(202) region of the nOP patterns in **Figure 6** (repeated bending around 10 mm diameter), showing the expected drop in (211) intensity as C replaces A after *convex* bending, with subsequent recovery of the (211) (and of A) after *concave* bending.

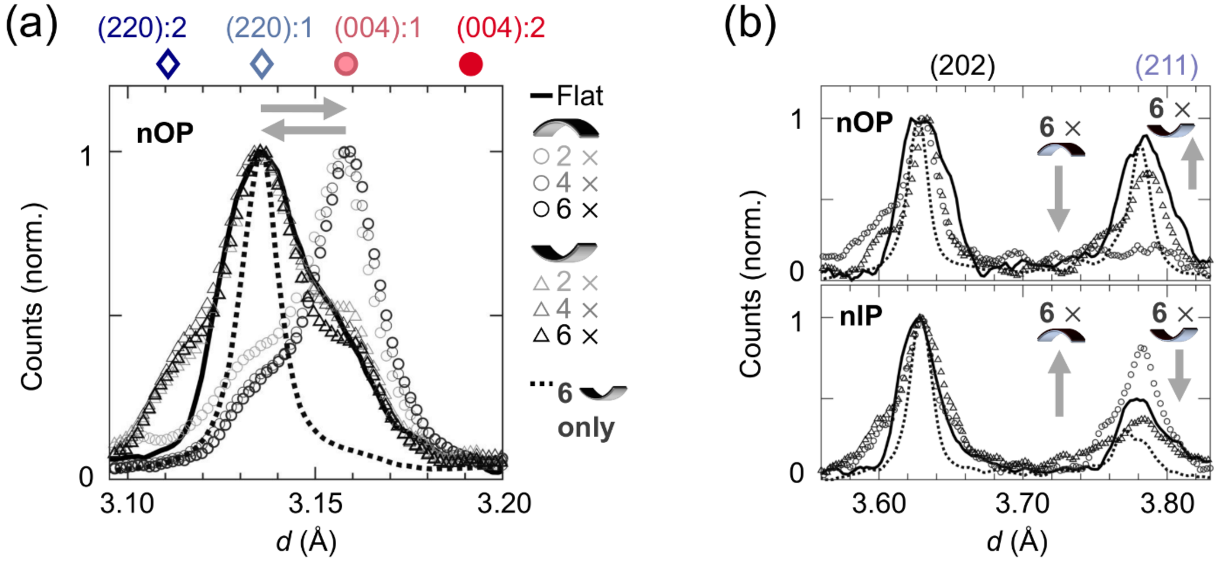

Figure S10. (a) GIWAXS nOP patterns in the (004)-(220) region for the successive *convex* and *concave* bending around a 4.1 mm diameter, as listed. (b) (221)-(202) region of select GIWAXS nOP and nIP linecuts.

Convex bending resulted in very large growth of the (004):1, with the main as-cast (220):1 peak considerably decreasing (**Figure 7a**). Correspondingly, the (211) strongly increased nIP and decreased nOP (**Figure S10b**). Subsequent *concave* bending resulted in an increase of the initial (220):1 peak, but with much (004):1 left over from the *convex* bending, and with a large and visible (220):2 shoulder. As expected, the (221) increased nOP and decreased nIP. Interestingly, when only *concave* bending was applied with no prior *convex* bending (called "*concave* bending only"), the (220):1 was practically the only peak observed, indicating mostly A:1. In this case, the (211) nIP is weaker than the (211) for the as-cast film, indicating more (004) nIP after 6 *concave* cycles only and therefore more (220) nOP. These striking changes are clear signs that much domain switching occurred during bending, with modifications made to the film being significantly retained when the applied strain was relieved.

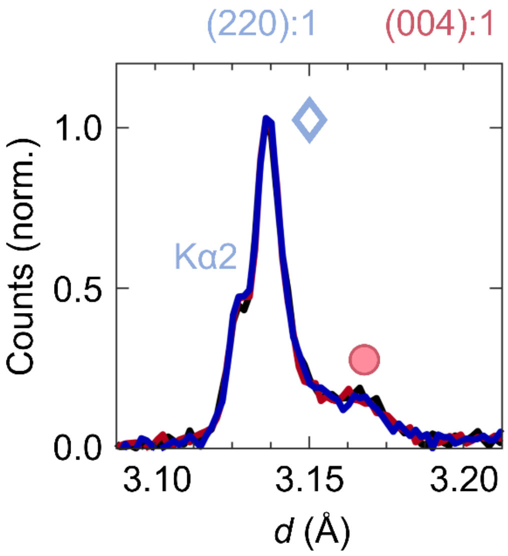

Figure S11. Three sequential powder XRD patterns (black, then red, then blue) of an as-cast $MAPbI_3$ film in the (220)-(004) region, showing a lack of change, and thus, stability under the beam.

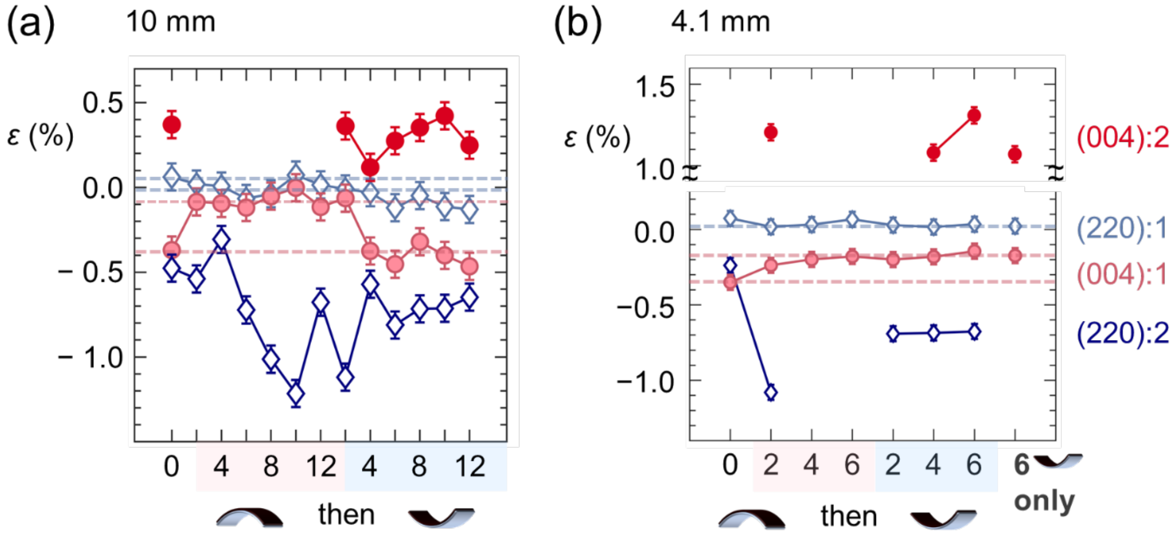

Figure S12. Evolution of (220) and (004) strains after the (a) 10 mm bending cycles and (b) 4.1 mm bending cycles.

Some changes in strain for the (220) and (004) peaks were observed after bending. For the 10 mm experiment, these changes seemed to correlate with bending configuration (*convex* vs. *concave*). It is possible that inelastic strain was retained by the (220) and (004) planes of MAPbI$_3$ after the applied strain was released.

While extensive alignments and calibrations performed on multiple instruments enabled us to determine with certainty the strain values pre-bending (**Figure 3**), alignment difficulties encountered after bending made us hesitant to draw conclusions from the trends observed post-bending (**Figure S12**). The strains measured in GIWAXS were fairly close to the resolution of both the height alignment performed during data collection, and the chi-*q* alignment performed during data processing (a further alignment that is done to correct any potential insufficient alignments during data collection). Good agreement for strains of the flat (pre-bent) samples measured via GIWAXS (**Figure 3**) and via lab XRD (on a variable-height stage) enabled us to conclude with confidence the values of the strains in **Figure 3**. Identification of different peaks post-bending was also obvious, such as the growth of the (004):1 peak in **Figures 6** or **8**. However, because the substrate was a very flexible polymer film, the precise locations of the different (220) and (004) peaks were less certain post-bending, even with all alignments, corrections, and various other measurement tricks (e.g. a very slightly sticky stage). For this reason, we included here the measured strains should the reader be curious, but do no extensively comment. We did not analyze the strain evolution of the (110)/(002) or (330)/(004) because the (110) and (002) peaks significantly overlapped with each other and the (330) and (006) peaks significantly overlapped with substrate peaks, so the (220) and (004) peaks were best for strain calculations.

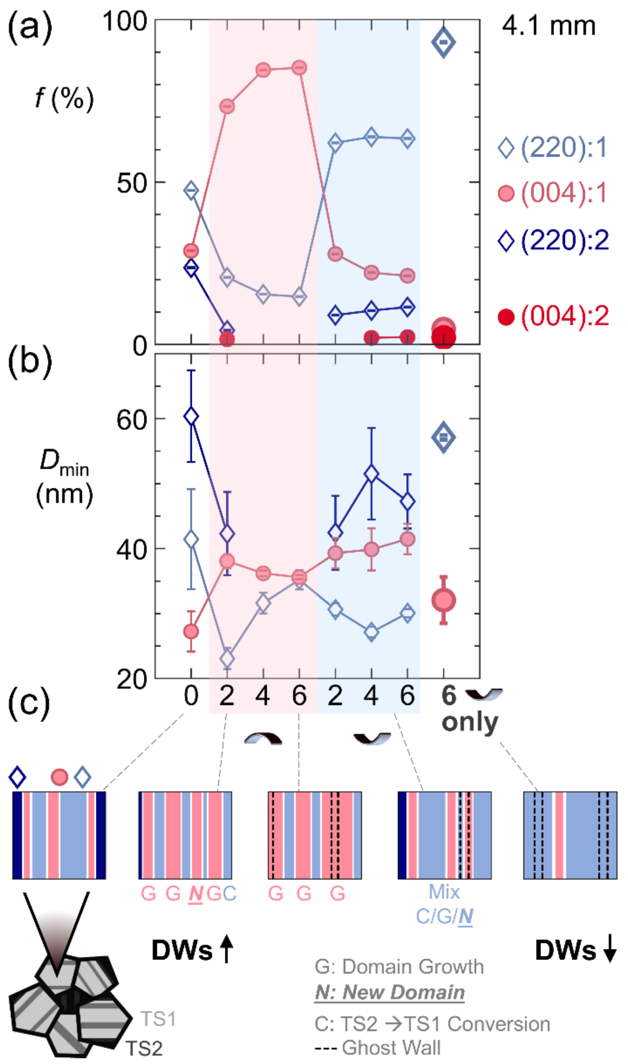

Figure S13. 4.1 mm bending experiment. Corrected fractions of total scattered intensity *f* (uncertainties < 0.1 %) for nOP peaks in the (220)-(004) region. (b) changes in minimum domain size D_{min} for the (220):1, (004):1, (220):2 and (004):2 peaks of nOP patterns (see **Figure 7**). (c) Summary schematics of the processes occurring during the 4.1 mm diameter bending experiments, with the evolution in the number of domain walls (DWs) listed. TS stands for Twin Set. For clarity, only the prior locations of walls that disappeared are shown as ghosts, rather than the prior locations of *both* walls that moved and walls that disappeared.

Changing the Number of Domain Walls during Bending (4.1 mm).

We examined changes to the minimum domain size D_{min} for the 4.1 mm bending experiment (**Figure 7**) in more detail, to see if the walls only moved, or if walls were created/annihilated as well. We caution that this study provides estimations only, as the effects of strain are not decoupled from peak width, over multiple peaks; but the analysis below is consistent with prior microscopy work. [5] We focus on TS1, as the peaks in TS2 were quite weak. *Convex* bending induces more C, and *concave* bending induces more A (**Figures 5, 6** and **S13**), due to wall movement. Thus, if we only have wall movement, C domains should become bigger after *convex* bending and A domains should become bigger after *concave* bending. However, if new C domains nucleate during *convex* bending, the size of C should decrease. These trends should also apply to the *minimum* size D_{min}, estimated using Scherrer broadening analysis (see above). Rapid growth of nucleated domains might mean that D_{min} of C decreases only slightly, as opposed to sharply decreasing. With respect to the minimum size specifically, if many C domains are annihilated during *concave* bending, the D_{min} of A domains will likely increase significantly. Such domain nucleation/annihilation is necessarily accompanied by an increase/decrease in the number of domain walls. In $\mathrm{MAPbI_3}$ under applied stress, both domain nucleation and annihilation have been observed, so we know that large changes to the number of domain walls is possible. [5]

Changes in D_{min} revealed both wall movement and creation/annihilation (**Figure S13b-c**). D_{min} of C:1 increased after 2 cycles of *convex* bending, and D_{min} of A:1 dropped. Thus, the walls moved through A:1s to increase the sizes of C:1s. This is reflected in the large increase in fraction of C:1 (**Figure S13a**). The minimum size of C:1 then decreased (cycles 4-6) while fraction of C:1 continued to increase, suggesting C:1 nucleation upon further *convex* bending, and thus, more walls. Curiously, the D_{min} of A:1 concurrently increased. This suggests annihilation of the smallest A:1 domains as walls move from C:1s. The mixture of wall movement with wall creation/annihilation during *convex* bending/unbending is consistent with previous microscopy observations made on $\mathrm{MAPbI_3}$ single crystals.[5] This process of wall movement/creation/annihilation appeared to be reversed with subsequent *concave* bending: D_{min} of A:1 decreased, suggesting A:1 nucleation. D_{min} of C:1 increased slightly but stayed within measurement uncertainty, suggesting slight C:1 annihilation. In the case of *concave* bending only (no prior *convex* bending), the minimum domain size of A:1 was 57.1 ± 0.4 nm, which is substantially larger than the range of as-cast domain sizes for A:1 (38 ± 4 nm, 4 samples). This result combined with the 95 % proportion of A:1 (**Figure S13a**) suggests the microstructure shown in **Figure S13c**, in which large A:1s are separated by very few C:1s, with very few domain walls total in the grain. Such a microstructure would result from progression of walls from A:1s through most C:1s such that many walls are annihilated, and large A:1s remain. Again, this behavior is consistent with observations of wall annihilation under *concave* bending in single crystals. [5] Thus, *convex* bending resulted in both wall creation and annihilation, while *concave* bending only seemed to favor annihilation.

REFERENCES

(1) Kennard, R. M.; Dahlman, C. J.; Nakayama, H.; Decrescent, R. A.; Schuller, J. A.; Seshadri, R.; Mukherjee, K.; Chabinyc, M. L. Phase Stability and Diffusion in Lateral Heterostructures of Methyl Ammonium Lead Halide Perovskites. *ACS Appl. Mater. Interfaces* **2019**, *11* (28), 25313-25321.

(2) Whitfield, P. S.; Herron, N.; Guise, W. E.; Page, K.; Cheng, Y. Q.; Milas, I.; Crawford, M. K. Structures, Phase Transitions and Tricritical Behavior of the Hybrid Perovskite Methyl Ammonium Lead Iodide. *Sci. Rep.* **2016**, *6* (June), 1-16.

(3) Birkholz, M.; Fewster, P. F.; Genzel, C. *Thin Film Analysis by X-Ray Scattering*; WILEY-VCH Verlag GmbH & Co. KGaA: Weinheim, Germany, 2006.

(4) Venkatesan, N. R.; Labram, J. G.; Chabinyc, M. L. Charge-Carrier Dynamics and Crystalline Texture of Layered Ruddlesden-Popper Hybrid Lead Iodide Perovskite Thin Films. *ACS Energy Lett.* **2018**, *3* (2), 380-386.

(5) Strelcov, E.; Dong, Q.; Li, T.; Chae, J.; Shao, Y.; Deng, Y.; Gruverman, A.; Huang, J.; Centrone, A. $CH_3NH_3PbI_3$ Perovskites: Ferroelasticity Revealed. *Sci. Adv.* **2017**, *3* (4), e1602165.

(6) Smilgies, D. M. Scherrer Grain-Size Analysis Adapted to Grazing-Incidence Scattering with Area Detectors. *J. Appl. Crystallogr.* **2009**, *42* (6), 1030-1034.

(7) WILSON, J. I. L. A. A. J. C. Seherrer after Sixty Years: A Survey and Some New Results in the Determination of Crystallite Size. *J. Appl. Crystallogr.* **1978**, *11*, 102-113.

(8) Suo, Z.; Ma, E. Y.; Gleskova, H.; Wagner, S. Mechanics of Rollable and Foldable Film-on-Foil Electronics. *Appl. Phys. Lett.* **1999**, *74* (8), 1177-1179.

(9) Sun, S.; Fang, Y.; Kieslich, G.; White, T. J.; Cheetham, A. K. Mechanical Properties of Organic-Inorganic Halide Perovskites, $CH_3NH_3PbX_3$ (X = I, Br and Cl), by Nanoindentation. *J. Mater. Chem. A* **2015**, *3* (36), 18450-18455.

(10) Rakita, Y.; Cohen, S. R.; Kedem, N. K.; Hodes, G.; Cahen, D. Mechanical Properties of $APbX_3$ (A = Cs or CH_3NH_3; X = I or Br) Perovskite Single Crystals. *MRS Commun.* **2015**, *5* (4), 623–629.

(11) Spina, M.; Karimi, A.; Andreoni, W.; Pignedoli, C. A.; Náfrádi, B.; Forró, L.; Horváth, E. Mechanical Signatures of Degradation of the Photovoltaic Perovskite $CH_3NH_3PbI_3$ upon Water Vapor Exposure. *Appl. Phys. Lett.* **2017**, *110* (12).

(12) Feng, J. Mechanical Properties of Hybrid Organic-Inorganic $CH_3NH_3BX_3$ (B = Sn, Pb; X = Br, I) Perovskites for Solar Cell Absorbers. *APL Mater.* **2014**, *2* (8).

(13) Okuzaki, H.; Ishihara, M. Spinning and Characterization of Conducting Microfibers. *Macromol. Rapid Commun.* **2003**, *24* (3), 261-264.